



HAL
open science

Kriging metamodels-based multi-objective shape optimization applied to a multi-scale heat exchanger

Franck Mastrippolito, Stéphane Aubert, Frédéric Ducros

► **To cite this version:**

Franck Mastrippolito, Stéphane Aubert, Frédéric Ducros. Kriging metamodels-based multi-objective shape optimization applied to a multi-scale heat exchanger. *Computers & Fluids*, 2021, 221, pp.104899. 10.1016/j.compfluid.2021.104899 . hal-03184653

HAL Id: hal-03184653

<https://hal.science/hal-03184653>

Submitted on 15 Mar 2023

HAL is a multi-disciplinary open access archive for the deposit and dissemination of scientific research documents, whether they are published or not. The documents may come from teaching and research institutions in France or abroad, or from public or private research centers.

L'archive ouverte pluridisciplinaire **HAL**, est destinée au dépôt et à la diffusion de documents scientifiques de niveau recherche, publiés ou non, émanant des établissements d'enseignement et de recherche français ou étrangers, des laboratoires publics ou privés.



Distributed under a Creative Commons Attribution - NonCommercial 4.0 International License

Kriging metamodels-based multi-objective shape optimization applied to a multi-scale heat exchanger

Franck MASTRIPPOLITO^{a,b}, Stéphane AUBERT^{a,*}, Frédéric DUCROS^b

^aUniv. Lyon, Ecole Centrale de Lyon, Laboratoire de Mécanique des Fluides et d'Acoustique UMR5509, Ecully, France

^bUniv. Grenoble Alpes, CEA, LITEN, DTBH, Laboratoire Echangeurs et Racteurs, Grenoble, France

Abstract

Heat exchanger behaviour is a multi-scale issue where local scale enhancement mechanisms coexist with global scale distribution ones. The present work investigates a multi-objective shape optimization of a heat exchanger. The proposed method is sufficiently robust to address multi-scale issues and allows industrial applications. Heat exchanger performances are evaluated using computational fluid dynamics (CFD) simulations. A genetic algorithm coupled with a Kriging-based metamodeling are used as optimization tools. Clustering and Self-Organizing Maps (SOM) are used to analyse the optimization results.

A metamodel builds an approximation of a simulator response (CFD) whose evaluation cost is reduced to be used together with genetic algorithm. An adaptive sampling is used to build cheap and precise approximations. The present optimization method is applied to a plate heat exchanger which constitutes a representative example of the aforementioned multi-scale aspects.

The results show that the metamodeling is a paramount element of the method, ensuring the robustness and the versatility of the optimisation process. Additionally, it allows to build correlations of the local scale used to determine the global performances of the heat exchanger. The clustering and the SOM highlight a finite number of shapes, which represent a compromise among the antagonist objective functions, tailoring the method to an industrial context.

Keywords: Kriging, Multi-objective Optimization, Adaptive sampling, Self-Organizing Maps, CFD, Heat exchanger, Multi-scale modelling

*Corresponding author

Email address: stephane.aubert@ec-lyon.fr (Stéphane AUBERT)

1. INTRODUCTION

Heat exchangers (HEX) are technological devices used to transfer thermal energy between two or more fluids. They are widely used in many industrial fields such as energy production (nuclear, fossil or renewable power plants), process industries, transports (automotive, aeronautics), cryogenics application or air conditioning [82]. Thus, performances optimization of heat exchangers is a transversal subject for energy transition and an efficient use of energy. These performances are related to the heat transfer rate and the pumping power required for the fluids flow.

These performances are directly linked to the shape of the heat exchanger and/or of its constitutive elements. Therefore, it seems that among the different existing ways to classify heat exchangers, the classification according to their construction is the most suitable for shape optimization. This classification allows to distinguish between two major types of heat exchangers¹: (1) *tubular heat exchangers* and (2) *plate heat exchangers*. The former category groups the heat exchangers for which at least one fluid flows throughout tubes. The tubes bundle is held by a shell or fins. These heat exchangers are versatile as they can work with different type of fluids and pressure levels. The heat exchangers of the latter category are formed by a stack of plates, usually corrugated, hence their compactness which is an advantage in several applications. For each heat exchanger type, different *passive* methods² are used to enhance the heat transfer by adding elements either into the tube and/or over the plates [45]. The purpose of these elements is multiple: (1) perturbing the flow and creating re-attachment points as well as recirculation zones; (2) increasing the heat exchange surface (fins) and (3) creating secondary vortices into the flow. The shape of the elements is therefore of major influence for the performances. These performances are also dependent on the *flow maldistribution* which happens in practice because of the manifold geometry or operating conditions (fluids viscosity for instance) [74].

The above paragraph clearly highlights the multi-scale behaviour of the heat exchanger. In order to analyse the different (coupled) phenomena taking place in, three geometrical scales must be defined: (1) the **global scale**, characterised by the heat exchanger dimensions (length, width, height) and the number of tubes and plates, allows to evaluate global performances; (2) the **channel scale**, characterized by the channel length, permits to consider flow establishment issues and (3) the **local scale**, characterized by the channel hydraulic diameter, is used to investigate heat transfer enhancement, flow recirculation and boundary layers evolutions.

In the context of shape optimization, the heat exchanger performances are usually obtained through analytical or numerical methods. Among these methods, computational fluid dynamics (CFD) is rising in importance because

¹Some references ([82] for instance) add a third category named *extended surface heat exchanger*. In the present work, this category is considered as a special case within the two others.

²Active methods also exist but they require an additional power input like jets or ultrasound for instance [10].

it provides access to velocity, pressure and temperature fields [79, 4]. However, the entire heat exchanger is rarely simulated through this way due to its high computational cost. In industrial applications, **the global methods, which determine the heat exchanger performances knowing the geometry and inlet/outlet conditions**, are often preferred for the global scale [31]. Then CFD is used to determine behaviour laws of heat exchange and drag coefficients of the elements at the local scale, which are then applied into the former method [1, 48]. Some authors [53, 30, 56] have also considered a porous approach to estimate the performances of the entire heat exchanger. At the local scale, the performances are expressed through the heat transfer and the drag coefficient, while at the global scale, the effectiveness of the heat exchanger and the total pressure drop are meaningful.

During the two last decades, shape optimization of heat exchanger has become a topic of major interest. Before 2010, optimization studies had been essentially mono-objective ones, performed by aggregating the several objectives into a single objective function. **But since the development of new algorithmn, the multi-objective optimization is invertigate. Most studies aim to optimize the heat exchanger performances through modifying the shape of the fins [52, 71, 72, 40, 43]. However, this shape is related to the global performance thanks to experimental correlations, which limit drastically the exploration of new untested shapes.**

At the same time, local scale shape optimizations were carried out using CFD, in order to overcome the shape limitations induced by the experimental correlations [36, 58, 70, 86, 39, 48] . Using CFD calculations for these studies leads to important computational cost justifying the use of *metamodels*, **which are matematical abstraction approximating the solver response [66]** . The Kriging method [66] is widely to built the metamodels is such studies. However, in the best knowledge of the authors most optimization studies use a designs of experiments with a priori fixed number of observations, which can limit the accuracy of the metamodels. Only few studies use adaptive strategy [70, 39, 48].

More recently, some studies have investigate the **heat exchanger manifold shape optimization [70, 38, 75]. These studies are based on CFD calculations alimenting metamodels for the optimisation. The classical multiple objectives are the pressure drop and the standard deviation of mass flow rate in each channel. Nevertheless, although relevant, none of these studies jointly consider the manifold impact on the heat exchanger effectiveness and pressure drop.**

As the previous paragraph points out, there are many studies on shape optimization at local or global scales, but very few investigate the impact of local shape variations on the overall heat exchanger performances. Habbadollahi *et al.* [26] determined the local performances (Colburn number and friction factor) of triangular fins using CFD simulations. Then, a model of a plate-fin heat exchanger is built using **a global method (ϵ -NTU)** to evaluate the global performance. The coupling is achieved by using two artificial neural networks-based metamodels. The metamodels behaviour is validate against experimental results. **Finally, the multi-objective optimisation (maximize the effectiveness and minimize the pressure drop) of the entire heat exchanger is performed by varying the triangular fins shape.** Abdelaziz *et al.* [1] and Yin and Ooka [87] used also similar approaches to investigate

local shape optimization impact on overall performances. More recently, Mastrrippolito *et al.* [48] have proposed a **multi-objective optimization aiming** to maximize the effectiveness while minimizing the pressure drop of a plate heat exchanger. The plates are mounted with rib-roughened plates. The heat exchanger is modelled by means of a multiscale approach. Kriging-based metamodels alimented by CFD are used to forward local performances to a global ε -NTU method. Then NSGA-II is used to determine the optimal solutions. Contrary to most studies, the design of experiment is not only built with a finite number of observations, but also through *adaptive sampling*, which produces accurate and cheaper metamodels by selecting only appropriate observations [22].

Considering the previous state of art, some limitations can be highlighted concerning the **multi-objective** shape optimization of heat exchanger: (1) the physical phenomena involved in a heat exchanger operation are highly multi-scale (local, global, manifold) but they are very rarely taken into account together in the context of optimization; (2) Kriging-based metamodels are used, but the advantages of the probabilistic formalism of the method, allowing adaptive sampling for instance, are rarely exploited; (3) most of the studies limit the analysis of the multi-objective optimization results to the Pareto front and they do not describe **the population distribution in the parameter space related to it** .

Therefore, the aim of this paper is to provide a multi-objective shape optimization method dealing with both local and global scales using a CFD solver **and Kriging metamodels**. **Indeed, the two scales have to be taken into account conjointly to handle their own specificities. Moreover, to do so without increasing drastically the computational cost, adaptive sampling strategies are used, benefiting from the aerodynamic community experience [33, 22, 41, 76] with a aim to extend their use to the heat exchanger community** . The multi-objective optimization is carried out using the classical genetic algorithm NSGA-II of [15] and the results are post-processed using appropriate methods in order to analyse not only the Pareto front but also the shape parameters.

The first part of this paper is dedicated to review the optimization tools background (Kriging, genetic algorithm and post-processing method). The second part presents the heat exchanger CFD modelling by describing the different scales and the multi-scale approach. The third part details and analyses the construction of the **metamodels** of the local scale. Finally, the heat exchanger multi-scale and multi-objective optimization problem is introduced, solved and analysed in the last part.

2. OPTIMIZATION TOOLS

2.1 Multi-objective problem

Solving a multi-objective optimization problem (MOP) consists in finding the vector of parameters which minimizes each component of a vector of objective functions. It may be written as follows [14, pp. 13]:

$$\min_{\mathbf{p} \in \mathcal{D}} \mathbf{y}(\mathbf{p}) \quad (1)$$

with

- the vector ³ of N_{obj} objective $\mathbf{y}(\mathbf{p}) = [y_i(\mathbf{p})]_{1 \leq i \leq N_{obj}} \in \mathbb{R}^{N_{obj}}$,
- the line vector of N_d parameters $\mathbf{p} = [p_i]_{1 \leq i \leq N_d}^T \in \mathcal{D}$

The problem is defined into two different spaces, the parameter space \mathcal{D} and the objective space \mathcal{F} defined as [46]:

$$\mathcal{D} = \left\{ \mathbf{p} \mid \mathbf{g}(\mathbf{p}) \leq 0; \mathbf{n}(\mathbf{p}) = 0; \mathbf{p}^{(L)} \leq \mathbf{p} \leq \mathbf{p}^{(U)} \right\} \quad (2)$$

$$\mathcal{F} = \{ \mathbf{y}(\mathbf{p}) \mid \mathbf{p} \in \mathcal{D} \} \quad (3)$$

where $\mathbf{p}^{(L)}$ and $\mathbf{p}^{(U)}$ are the lower and upper limit of the parameter, $\mathbf{g}(\mathbf{p})$ is the vector of inequality constraints and $\mathbf{n}(\mathbf{p})$ is the vector of equality constraints.

The solution of this multi-objective problem is rarely unique and the multiple solutions form the best compromise between the several objectives, called the *Pareto front in the objective space* and the *Pareto set in the parameter space*.

In order to find the solution, the literature reports many tools and methods. However, the same term is sometimes used to describe different methods, or to gather several tools, which can lead to misunderstandings. The present paper proposes a clear classification of the different methods used into three groups :

- the *motors of optimization* which aim at finding the minimum of a single (or several) objective function using its value and its derivatives (if necessary). At least two categories can be distinguished: classical and meta-heuristic methods. The formers are essentially related to mono-objective problems. The most used are for instance: Newton method, Simplex method or conjugate gradient [13]. The meta-heuristic methods were developed to extend the range of approachable problems, in particular to multi-objective ones. They are based on a stochastic exploration of the parameter space. Genetic algorithms, whose popularity has constantly grown over the last few decades, belong to this category [14].
- the *conditioners* which transform the initial vector of objectives into a more suitable one for the motor. The most famous conditioner is the aggregate method [51] which creates an unique objective function through a weighted sum. These tools are optionals and closely related to the motor used.
- the *fuels for optimization* which give to the motor the value of the objective and its derivatives (if necessary) used to perform the minimization. Fuels can be classified into three groups (direct, gross and refined) depending on the nature of the information available. It is called direct when analytical expressions of the objectives are available. When only the value of the objective is known and no analytical expression exists,

³By default and without any further details, the vectors are column vectors.

the fuel is gross (CFD solvers are typical examples). When the information coming from gross fuel is treated by a mathematical and/or a physical process, the term "refined fuel" is employed. This is the case of the *metamodels* (or surrogate models), for instance.

In the present paper, the used motor is a multi-objective genetic algorithm. Thus, the conditioner is not mandatory and the identity operator is chosen. A CFD solver is used as gross fuel and it is refined through Kriging-based metamodels. The choice of these tools is presented thereafter.

2.2 Motor of optimization: NSGA-II

Genetic algorithms are based on the Darwin's theory of evolution. At each generation, the population of individuals is more and more adapted to its environment. **These algorithms mimic the evolution process consisting in changing of the individual's genes through reproduction, crossover and spontaneous mutation.**

Over the variety of algorithms available into the literature [24], the NSGA-II proposed by Deb *et al.* [15] was preferred. Indeed, it is employed in numerous studies in heat and fluid flow [72, 26, 78, 9, 48] due to its robustness and its capability to properly describe the Pareto front. The main particularities of this genetic algorithm are [15]: (1) the use of a probabilistic operator for the reproduction (*Simulated Binary Crossover*) and the mutation (*polynomial mutation*); (2) the selection step performed by means of a tournament and a *crowding distance* operator, which preserves the diversity of the individuals on the Pareto front.

A limitation of the genetic algorithms is the large number of individuals and generations needed to obtain properly described and converged Pareto set and front. If, as in the present work, the gross fuel is a CFD solver, the computational cost may be prohibitive for industrial applications as pointed out by Hilbert *et al.* [28]. Thus, the use of a set of metamodels as refined fuel is mandatory to make this optimization method suitable for an industrial context. The aim is to replace the costly CFD solver by a cheaper approximation, in the present work, a set of Kriging-based metamodels.

2.3 Refined fuel for optimization: Kriging metamodels

Kriging is a geostatistical interpolation method which was extended by Sacks *et al.* [68] to the field of deterministic function approximation under the name of Design and Analysis of Computer Experiments (DACE). It is a versatile method, allowing adaptive sampling and being able to estimate the likelihood of the approximation [66]. The universal Kriging is used in the present paper. A metamodel is built for an unique objective, so there are as many metamodels as objectives in the MOP. The result obtained thanks to the CFD solver is hereinafter called *response*.

2.3.1 Universal Kriging theory

The Kriging method treats the deterministic response y given by the CFD solver as a realization of the random Gaussian process $\{Y(\mathbf{p})\}_{\mathbf{p} \in \mathcal{D}}$ defined as the sum of a deterministic part and a stochastic one. For a given vector of parameters $\mathbf{p} \in \mathcal{D}$, the approximation is written as:

$$Y(\mathbf{p}) = v(\mathbf{p}) + Z(\mathbf{p}) \quad (4)$$

The deterministic trend $v : \mathbf{p} \in \mathcal{D} \rightarrow v(\mathbf{p}) \in \mathbb{R}$ is a weighted sum of the N_b known basis functions v_i :

$$v(\mathbf{p}) = \sum_{i=1}^{N_b} \beta_i v_i(\mathbf{p}) \quad (5)$$

The centered stationary random Gaussian process $\{Z(\mathbf{p})\}_{\mathbf{p} \in \mathcal{D}}$ has zero mean and a stationary covariance kernel expressed as :

$$K(\mathbf{p}^{(1)}, \mathbf{p}^{(2)}) = \sigma^2 R(\mathbf{p}^{(1)}, \mathbf{p}^{(2)}, \boldsymbol{\theta}) \quad (6)$$

being σ the Gaussian process variance, R the spatial correlation function and $\boldsymbol{\theta} \in \mathbb{R}^{N_d}$ the vector of *characteristic length-scales* [66]. The components of the length-scales vector have the same units as the corresponding ones of the vector of parameters \mathbf{p} . The correlation function R is obtained as the tensorial product of stationary mono-dimensional function depending on the Euclidean distance between two parameters [66] :

$$R(\mathbf{p}^{(1)}, \mathbf{p}^{(2)}, \boldsymbol{\theta}) = \prod_{k=1}^{N_d} \tilde{R}(p_k^{(1)} - p_k^{(2)}, \theta_k) \quad (7)$$

with $p_k^{(\cdot)}$ and θ_k , the k^{th} component of the vectors \mathbf{p} and $\boldsymbol{\theta}$.

Building the Kriging metamodel consists in estimating the following unknowns: $\boldsymbol{\beta}$, σ and $\boldsymbol{\theta}$. To do so, a design of experiments (DOE) is necessary. For a unique response y , a DOE of N_o observations is composed by a matrix of parameters \mathbf{P} and the corresponding vector of responses \mathbf{y} , defined as:

$$\mathbf{P} = \left[\mathbf{p}^{(i)} \right]_{1 \leq i \leq N_o} \in \mathcal{D}^{N_o} \quad (8)$$

$$\mathbf{y} = \left[y(\mathbf{p}^{(i)}) \right]_{1 \leq i \leq N_o} \in \mathbb{R}^{N_o} \quad (9)$$

where $\mathbf{p}^{(i)}$ is the i^{th} vector of parameters in the DOE and $y(\mathbf{p}^{(i)})$ is the CFD solver response associated. **From this DOE, the Kriging approximation is given by the Kriging mean**, expressed as [66, 8]:

$$m_K(\mathbf{p}) = \mathbf{v}(\mathbf{p})^T \hat{\boldsymbol{\beta}} + \mathbf{r}(\mathbf{p})^T \mathbf{R}^{-1} (\mathbf{y} - \mathbf{V} \hat{\boldsymbol{\beta}}) \quad (10)$$

The mean squared error (MSE) is the second order moment, expressed:

$$s_K^2(\mathbf{p}) = \hat{\sigma}^2 \left(1 - \mathbf{r}(\mathbf{p})^T \mathbf{R}^{-1} \mathbf{r}(\mathbf{p}) + (\mathbf{v}(\mathbf{p})^T - \mathbf{r}(\mathbf{p})^T \mathbf{R}^{-1} \mathbf{V})^T (\mathbf{V}^T \mathbf{R}^{-1} \mathbf{V})^{-1} (\mathbf{v}(\mathbf{p})^T - \mathbf{r}(\mathbf{p})^T \mathbf{R}^{-1} \mathbf{V}) \right) \quad (11)$$

Table 1: Comparison between metamodels predictions and CFD simulations for the five centres.

Symbol	Equation	Description
$\mathbf{v}(\mathbf{p})$	$[v_i(\mathbf{p})]_{1 \leq i \leq N_b}$	Basis functions vector
\mathbf{V}	$[v_j(\mathbf{p}^{(i)})]_{1 \leq i \leq N_o, 1 \leq j \leq N_b}$	Experimental matrix
$\mathbf{r}(\mathbf{p})$	$[R(\mathbf{p}, \mathbf{p}^{(i)}, \boldsymbol{\theta})]_{1 \leq i \leq N_o}$	Correlation vector between a given vector of parameters $\mathbf{p} \in \mathcal{D}$ and the vectors of parameters of the DOE \mathbf{P}
\mathbf{R}	$[R(\mathbf{p}^{(i)}, \mathbf{p}^{(j)}, \boldsymbol{\theta})]_{1 \leq i \leq N_o, 1 \leq j \leq N_o}$	Correlation matrix between the vectors of parameters of the DOE \mathbf{P}

The notation used in Eqs. (10) and (11) are summarized on Tab. 1. The predicted error variance $\hat{\sigma}^2$ (which is an estimation of σ^2), the vector of generalized least square estimates of the trend coefficient $\hat{\boldsymbol{\beta}}$ (estimation of $\boldsymbol{\beta}$) and the vector of characteristic length-scales $\boldsymbol{\theta}$ are unknowns to be estimated. They are determined thanks to the *maximum likelihood estimation* method. The analytical expressions for $\hat{\boldsymbol{\beta}}$ and $\hat{\sigma}^2$ are [57, 48]:

$$\hat{\boldsymbol{\beta}} = (\mathbf{V}^T \mathbf{R}^{-1} \mathbf{V})^{-1} \mathbf{V}^T \mathbf{R}^{-1} \mathbf{y} \quad (12)$$

$$\hat{\sigma}^2 = \frac{1}{N_o} (\mathbf{y} - \mathbf{V} \hat{\boldsymbol{\beta}})^T \mathbf{R}^{-1} (\mathbf{y} - \mathbf{V} \hat{\boldsymbol{\beta}}) \quad (13)$$

The vector of characteristic length-scales is obtained by minimizing the opposite of the *log-likelihood* function Park and Baek [57].

The Kriging approximation is illustrated in Fig. 1 for a sine function. The 95% confidence interval is computed from the mean squared error, and large areas depict unlikely approximation. This is the case for the unobserved region $p \in [0, \pi/2]$.

2.3.2 Nugget effect

By construction, the Kriging mean given by Eqn. (10) interpolates the observations of the DOE and the mean squared error given by Eqn. (11) is zero at these observations:

$$\forall \mathbf{p} \in \mathbf{P}, \quad m_K(\mathbf{p}) = y(\mathbf{p}) \quad (14)$$

$$s_K^2(\mathbf{p}) = 0 \quad (15)$$

This behaviour assumes that the CFD solver response is deterministic, that is tantamount to say that for the same vector of parameters at the input, the solver return always the same response. However, this is not always the case. Indeed, the response is susceptible to variate due to convergence issues. Moreover, some "jumps" of the response may appear [54, pp.23] because of numerical instabilities or due to the use of physical models outside their field of

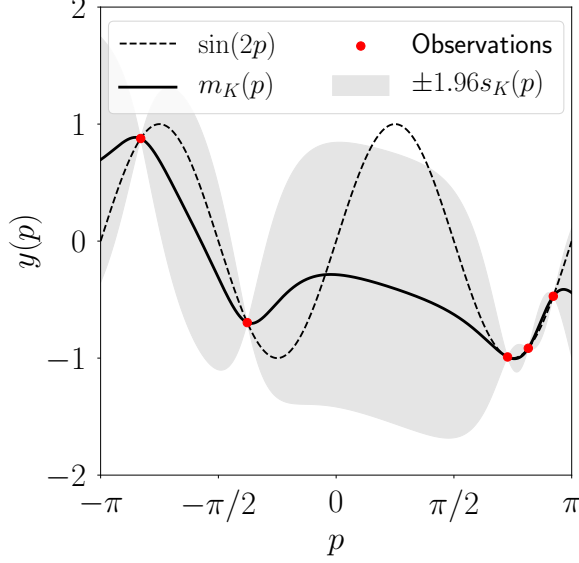


Figure 1: The Kriging mean (solid line) is an approximation of the true function (dashed line) built from five observations (red dots). The means squared error allows to build the 95% confidence interval (grey areas).

validity for certain vectors of parameters. To take into account those jumps, *nugget effect* is added to the Kriging metamodel by the way of a constant variance τ^2 appended to the covariance kernel:

$$K(\mathbf{p}^{(1)}, \mathbf{p}^{(2)}) = \sigma^2 R(\mathbf{p}^{(1)}, \mathbf{p}^{(2)}, \boldsymbol{\theta}) + \tau^2 \delta(\mathbf{p}^{(1)}, \mathbf{p}^{(2)}) \quad (16)$$

where $\delta(\cdot, \cdot)$ is the Kronecker symbol. Adding this effect leads to a modification in the estimations of the parameters $\boldsymbol{\beta}$, σ^2 and $\boldsymbol{\theta}$ and introduces the new unknown parameter τ^2 . The estimators $\hat{\boldsymbol{\beta}}$ and $\hat{\sigma}^2$ become:

$$\hat{\boldsymbol{\beta}} = (\mathbf{V}^T \mathbf{R}_\tau^{-1} \mathbf{V})^{-1} \mathbf{V}^T \mathbf{R}_\tau^{-1} \mathbf{y} \quad (17)$$

$$\hat{\sigma}^2 = \frac{1}{N_o} (\mathbf{y} - \mathbf{V} \hat{\boldsymbol{\beta}})^T \mathbf{R}_\tau^{-1} (\mathbf{y} - \mathbf{V} \hat{\boldsymbol{\beta}}) \quad (18)$$

where \mathbf{R}_τ is the modified correlation matrix:

$$\mathbf{R}_\tau = \frac{\sigma^2}{\sigma_\tau^2} \mathbf{R} + \frac{\tau^2}{\sigma_\tau^2} \mathbf{1}_{N_o} \quad (19)$$

with the total variance defined as $\sigma_\tau^2 = \sigma^2 + \tau^2$ and $\mathbf{1}_{N_o}$ being the identity matrix of size $N_o \times N_o$. The log-likelihood function is also modified. By solving the minimization problem of the opposite log-likelihood, the vector of characteristic length-scale $\boldsymbol{\theta}$ and the nugget effect variance τ^2 are obtained. It should be noted that as the nugget effect adds a constant variance directly to the covariance kernel, the Kriging mean is still interpolating the DOE observations.

2.3.3 Adaptive sampling

Sampling is a critical step in the building of metamodels. The number of observations and their position in the parameter space highly influence the quality of the approximation [63]. This is clearly highlighted in Fig. 1. Latin Hypercube Sampling (LHS) is one of the most used techniques to create design of experiments because of its versatility and its capability to generate non-redundant observations with a good *space filling* [84]. Moreover, many studies have proposed to optimize the position of the observations to increase the space filling [12]. However, even paying a close attention to this step, the optimum can be missed if there is no observations close to its position or can be biased if the space is not sufficiently described in its neighbourhood. Also, to ensure a good space filling, the number of observations needed is empirically estimate as $N_o \sim 10N_d$ [12]. In studies with numerous parameters and based on CFD solvers, it might be very difficult to follow this rule.

To overcome these issues and to built cheaper and more accurate metamodels, *adaptive sampling* methods are used [22]. Starting from an initial coarse DOE, new observations are iteratively added to it in order to improve: (1) the current optimal area which is related to the *exploitation* of the promising area; (2) the global accuracy of the metamodel, by performing an *exploration* of the parameter space. To achieve one or both of these targets, several *infill criteria* had been developed. They quantify the benefit of adding a new observation and allow to choose it adequately regarding the required target. The EGO algorithm introduced by Jones *et al.* [32] is a major reference for adaptive sampling. It is based on the *expected improvement* criteria which represents a compromise between exploration and exploitation.

Thanks to Kriging method formalism, a lot of different infill criteria were developed with their own advantages and drawbacks. In the present work, not only one but several criteria are used. The main idea is to benefit from the advantages and try to mitigate the drawbacks, as proposed by Liu *et al.* [42]. The multi-points expected improvement (q-EI), the maximum mean squared error (MMSE), the integrated mean squared error (IMSE), the expected hypervolume improvement (EHI) and the expected excursion volume (EEV) are used in this work and are presented thereafter.

Multi-points Expected improvement (q-EI). The expected improvement criterion has been proposed by Jones *et al.* [32]. It takes advantages of the probabilist formulation of the Kriging to calculate the expected improvement, which quantify for $\mathbf{p} \in \mathcal{D}$ the probable achieved improvement of the approximation if this observation is added to the DOE. The improvement function is defined as:

$$\mathcal{I}(\mathbf{p}) = \max(\min(\mathbf{y}) - Y(\mathbf{p}), 0) \quad (20)$$

where \mathbf{y} is given by Eqn. (9) and $Y(\mathbf{p})$ is a single realization of the random process defined in Eqn. (4). The expected improvement is the expectation of this function:

$$\text{EI}(\mathbf{p}) = \mathbb{E}[\mathcal{I}(\mathbf{p})|Y(\mathbf{P}) = \mathbf{y}] \quad (21)$$

$$\begin{aligned} &= (\min(\mathbf{y}) - m_K(\mathbf{p}))F_{\mathcal{N}(0,1)}\left(\frac{\min(\mathbf{y}) - m_K(\mathbf{p})}{s_K(\mathbf{p})}\right) \\ &\quad + s_K(\mathbf{p})f_{\mathcal{N}(0,1)}\left(\frac{\min(\mathbf{y}) - m_K(\mathbf{p})}{s_K(\mathbf{p})}\right) \end{aligned} \quad (22)$$

where $F_{\mathcal{N}(0,1)}(\cdot)$ and $f_{\mathcal{N}(0,1)}(\cdot)$ are the cumulative distribution function and the probability density function of the standard normal distribution. The compromise between exploitation (first term) and exploration (second term) is clearly shown in the Eqn. (22). This criterion is zero at the observations of the DOE and strictly positive elsewhere as shown in Fig. 2(a). Its value increases with $s_K^2(\cdot)$ and decreases with $m_K(\cdot)$. It has been widely used in several studies [73, 54]. It also provides a helpful quantification to stop the DOE enrichment.

But, this criterion is sequential. This means that it provides only a single observation to be added to the DOE. When CFD solvers are used to determine the response, sequential approaches are not suitable due to the important calculation time. Therefore, it is usually preferred to run several simulations at the same time. *Batch* infill criterion was developed in this way [25]. A set of q observations $\mathbf{P}_q \in \mathcal{D}^q$ is determined as:

$$\mathbf{P}_q = [\mathbf{p}^{(i)}]_{1 \leq i \leq q} \quad (23)$$

with $q \geq 2$. Ginsbourger *et al.* [25] have proposed a *multi-points expected improvement* (q-EI). Given \mathbf{P}_q and the vector of the realization $Y(\mathbf{P}_q)$, the q-EI is defined as the expectation of a joint improvement function:

$$\text{q-EI}(\mathbf{P}_q) = \mathbb{E}[\max(\min(\mathbf{y}) - \min(Y(\mathbf{P}_q)), 0) | Y(\mathbf{P}) = \mathbf{y}] \quad (24)$$

The set of observation \mathbf{P}'_q added to the DOE is determined in order to maximize this criterion:

$$\mathbf{P}'_q = \arg \max_{\mathbf{P}_q \in \mathcal{D}^q} \text{q-EI}(\mathbf{P}_q) \quad (25)$$

The q-EI yields an analytical expression only for $q = 2$. In other cases, an heuristic strategy called *Constant Liar* is used. It is based on the use of a *liar* to avoid interrogating the CFD solver. Once an observation is added to the DOE, the liar is applied as response. It is set to the current known minimum of \mathbf{y} . This criterion gives a valuable information about the joint probability of improving the optimum, but it depends on the number of observations q to add. A condition can also be developed to stop the adaptive sampling.

Maximum Mean Squared Error (MMSE). One of the main advantages of Kriging metamodels is their capability to estimate the prediction likelihood through the computation of the mean squared error $s_K^2(\mathbf{p})$. The main idea of the *maximum mean squared error* criterion is to add to the DOE the observation which maximises it [62]:

$$\mathbf{p}' = \arg \max_{\mathbf{p} \in \mathcal{D}} s_K^2(\mathbf{p}) \quad (26)$$

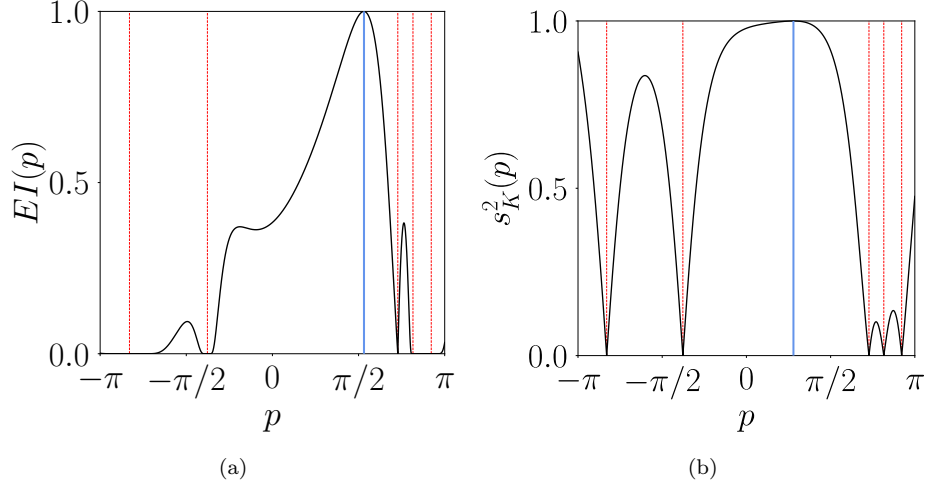


Figure 2: EI (a) and MMSE (b) infill criteria plots for the sine function of Fig. 1. The DOE observations position is indicated by the red dashed lines and the \mathbf{p}' position by the solid blue line.

If an infinity of observation are added through this exploration criterion, the resulting metamodel will have the better accuracy as defined by the root mean squared error (RMSE) [73]. However, as $s_K^2(\mathbf{p}) = 0, \forall \mathbf{p} \in \mathbf{P}$, the MSE is strongly multimodal, as shown in Fig. 2(b), and the maximization problem defined in Eqn. (26) is difficult and costly. Additionally, this criterion provides a local information of the approximation accuracy and leads usually to add observations at the boundaries of the parameter space. This criterion is also a sequential one. In order to benefit from batch simulations, a Constant Liar method can be applied to this criteria with a liar equal to the prediction value [48]. Regarding the adaptive sampling, MMSE is able to quantify the maximal uncertainty of the approximation that helps at stopping the DOE enrichment.

Integrated Mean Squared Error (IMSE). In order to overcome the local aspect of the MMSE criterion while benefiting from the exploration property, the IMSE criterion was proposed [67, 62]. It is defined as:

$$\text{IMSE} = \int_{\mathcal{D}} s_K^2(\mathbf{p}) d\mathbf{p} \quad (27)$$

It measures an average accuracy of the metamodel while the MMSE criterion measures the risk of maximal error of the metamodel prediction. The observation \mathbf{p}' added to the DOE is the one which minimizes the IMSE once added:

$$\mathbf{p}' = \arg \min_{\mathbf{p} \in \mathcal{D}} \int_{\mathcal{D}} s_K^2(\mathbf{p} | \{\mathbf{P}, \mathbf{p}'\}) d\mathbf{p} \quad (28)$$

where $s_K^2(\mathbf{p} | \{\mathbf{P}, \mathbf{p}'\})$ is the MSE of the metamodel built thanks to the DOE \mathbf{P} supplemented with the new observation \mathbf{p}' . This criterion does not focus on the actual benefit of adding an observation, but on a global reduction of the uncertainty. It is easily extended to a batch formulation [11]. The set of observations \mathbf{P}'_q , once

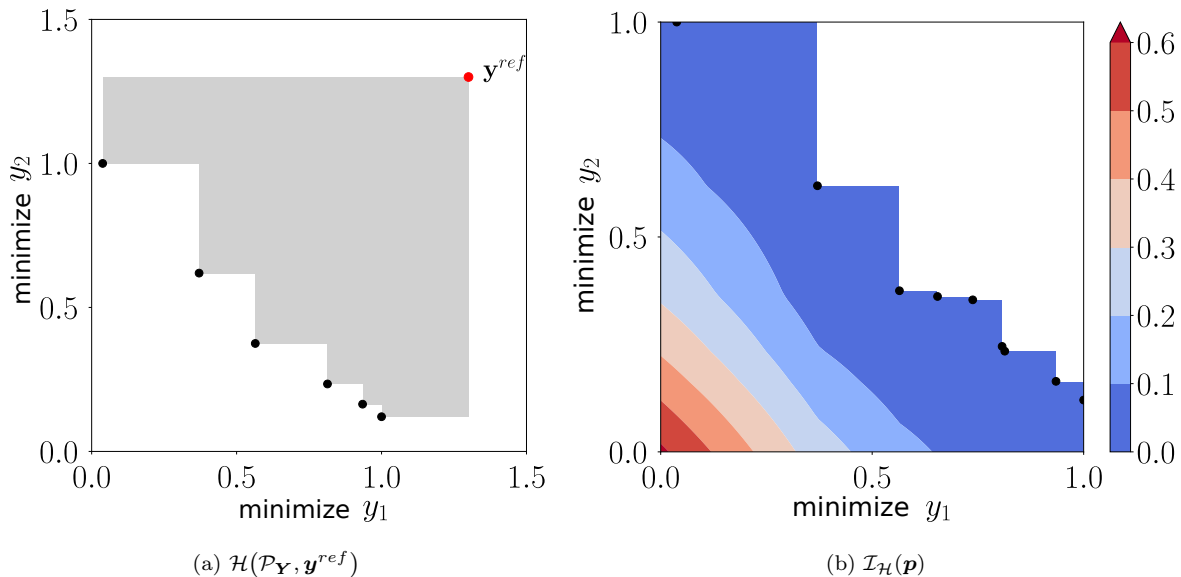


Figure 3: Bi-objective EHI illustration: (a) The hypervolume (grey area) is calculated between the non-dominated DOE observations (in black) and the reference point \mathbf{y}^{ref} in red. (b) Contour plot of the improvement function. The non-dominated DOE observations are in black and the reference point is $\mathbf{y}^{ref} = \{1.25, 1.25\}$.

added to the DOE, will minimize the IMSE and is given by:

$$\mathbf{P}'_q = \arg \min_{\mathbf{P}'_q \in \mathcal{D}^q} \int_{\mathcal{D}} s_K^2(\mathbf{p} | \{\mathbf{P}, \mathbf{P}'_q\}) d\mathbf{p} \quad (29)$$

Solving directly this optimization problem is numerically expensive. Thus an heuristic strategy like the Constant Liar one is often preferred.

The numerical cost of this criterion is an issue when the number of dimensions of the parameter space \mathcal{D} is significantly large [62].

Expected Hypervolume Improvement (EHI). With the development of multi-objective motors of optimization able to generate a Pareto front, new exploitation criteria were introduced in order to enrich the DOE by taking into account the compromise between the different objectives. The sequential criterion EHI proposed by [20] is one of them. It can be interpreted as an extension of the expected improvement to multi-objective problems [80]. The improvement function is modified such as [20, 19]:

$$\mathcal{I}_{\mathcal{H}}(\mathbf{p}) = \begin{cases} 0 & \text{if } \mathcal{P}_{\mathbf{Y}} \preceq \mathbb{Y}(\mathbf{p}) \text{ or } \mathbf{y}^{ref} \preceq \mathbb{Y}(\mathbf{p}) \\ \mathcal{H}(\mathbb{Y}(\mathbf{p}) \cup \mathcal{P}_{\mathbf{Y}}, \mathbf{y}^{ref}) - \mathcal{H}(\mathcal{P}_{\mathbf{Y}}, \mathbf{y}^{ref}) & \text{else} \end{cases} \quad (30)$$

where $\mathcal{H}(\mathcal{P}_{\mathbf{Y}}, \mathbf{y}^{ref})$ is the measure of the hypervolume between the non-dominated observations of the DOE $\mathcal{P}_{\mathbf{Y}}$ (assumed to be the better representation of the Pareto front), and a reference point \mathbf{y}^{ref} [20]. In two-dimensional

spaces it is equivalent to the area, as visible in Fig. 3(a). The improvement is calculated in the objective space and it is illustrated in Fig. 3(b). The maximal improvement is achieved for the furthest area from the DOE observations. The EHI is the expectation of this function knowing the DOE:

$$\text{EHI}(\mathbf{p}) = \mathbb{E} [\mathcal{I}_{\mathcal{H}}(\mathbf{p}) | \mathbb{Y}(\mathbf{P}) = \mathbf{Y}] \quad (31)$$

where $\mathbb{Y}(\mathbf{P})$ is the vector of the realizations of the random processes approximating $\mathbf{y}(\mathbf{p})$:

$$\mathbb{Y}(\mathbf{p}) = [Y_i(\mathbf{p})]_{1 \leq i \leq N_{obj}} \quad (32)$$

The new observation added to the DOE that will maximize this expectation is given by:

$$\mathbf{p}' = \arg \max_{\mathbf{p} \in \mathcal{D}} \text{EHI}(\mathbf{p}) \quad (33)$$

When $N_{obj} > 2$, the EHI cannot be estimated analytically and an heuristic algorithm is used, involving a significant numerical cost [80].

Expected Excursion Volume (EEV). The majority of the exploitation criteria are based on adding new observations at the probable position of the optimum. Villemonteix *et al.* [85] have tried to express the problem in a different way: which observations are relevant to increase the knowledge about this optimum? Thus, they have proposed a criterion measuring the uncertainty of the optimum position (for a mono-objective problem): the lower the value is, the better the optimum is located. Based on the same idea Picheny [61] has proposed to quantify this uncertainty through an *excursion volume*. For a multi-objective problem, it is calculated as the integral of the probability that the vector of objectives $\mathbf{y}(\mathbf{p})$ is non-dominated by the non-dominated observations of the DOE $\mathcal{P}_{\mathbf{Y}}$:

$$ev(\mathbf{p}) = \int_{\mathcal{D}} \mathbb{P}[\mathbf{y}(\mathbf{p}) \not\leq \mathcal{P}_{\mathbf{Y}} | \mathbb{Y}(\mathbf{P}) = \mathbf{Y}] d\mathbf{p} \quad (34)$$

If $ev(\mathbf{p})$ is small, $\mathcal{P}_{\mathbf{Y}}$ is probably close to the "true" Pareto front. The infill criteria is based on the reduction volume benefit provided by the new observation \mathbf{p}' added to the DOE written as [61]:

$$\text{EEV}(\mathbf{p}') = \mathbb{E} \left[\int_{\mathcal{D}} \mathbb{P}[\mathbf{y}(\mathbf{p}) \not\leq \{\mathcal{P}_{\mathbf{Y}} \cup \mathbb{Y}(\mathbf{p}')\} | \{\mathbb{Y}(\mathbf{P}) = \mathbf{Y}, \mathbb{Y}(\mathbf{p}') = \mathbf{Y}_{n+1}\}] d\mathbf{p} \right] \quad (35)$$

with $\mathbf{Y}_{n+1} \sim \mathcal{GP}(\mathbf{m}_{\mathbf{K}}(\mathbf{p}'), \mathbf{s}_{\mathbf{K}}^2(\mathbf{p}'))$ being the Gaussian process realization associated to the new observation, defined by solving the following minimization problem:

$$\mathbf{p}' = \arg \min_{\mathbf{p} \in \mathcal{D}} \text{EEV}(\mathbf{p}) \quad (36)$$

In the same way that the IMSE criterion, the numerical cost is significant when the number of dimensions of the parameter space \mathcal{D} is large. However, it has the intrinsic advantage of being independent of the scale differences between the objectives [61].

Stop condition The adaptive sampling is used in practice to built accurate metamodels with a limited number of observations. In industrial cases, this limit is imposed by both the calculation resources available and the time dedicated to the study. The choice of a relevant stop condition is still an open question [62].

As mentioned, the q-EI and MMSE criteria give information allowing the definition of a stop condition. Inspired by the EI condition exposed by Huang *et al.* [29], the present work suggests to use the following condition for q-EI:

$$\frac{1}{|\max(\mathbf{y}) - \min(\mathbf{y})|} \frac{\text{q-EI}(\mathbf{P}'_q)}{q} \leq \delta_{\text{q-EI}} \quad (37)$$

When the left hand side of Eqn. (37) is smaller than the tolerance $\delta_{\text{q-EI}}$, the numerical cost of finding new observations is too high in regards to the potential benefits. For the MMSE, the classical condition is expressed as [48]:

$$\frac{s_K^2(\mathbf{p}')}{|\max(\mathbf{y}) - \min(\mathbf{y})|} < \delta_{\text{MMSE}} \quad (38)$$

where \mathbf{p}' is the last observation added by the Constant Liar.

The information provided by the IMSE, EHI and EEV criteria are not relevant to build a stopping condition. When they are used, a maximal number of observations is prescribed.

2.4 Analysis tools

Two different analysis tools are used in the present work. The first one aims at highlighting a finite number of shapes, relevant for industrial purposes. The second one is used to visualize data generated by the optimization process.

2.4.1 Clustering

When a genetic algorithm is used as a motor of optimization, the number of optimal solutions is equal to the number of individuals in the population. Thus, it would be difficult in an industrialization process to select a unique optimal shape over several hundreds. As proposed by Kim *et al.* [35], *clustering* techniques may be used to extract a limited number of shapes from the optimal solutions. The main idea of these methods is to classify the population into distinct groups, each of them containing homogeneous individuals. Therefore, the group is represented by a *center of the group*, generalizing the main characteristics of the grouped individuals.

There exists numerous methods to do so. Kim *et al.* [35] proposed the *K-means* clustering which is easily implementable. Indeed, homogeneity between individuals is measured thanks to the Euclidean distance between an individual and the center of the group, defined as the barycentre of the grouped individuals. However, this measure can create groups which are not "visually" correct. Moreover as the number of employed groups has to be set by the user beforehand, there is a risk of over-partitioning the population.

Because of these limitations, *Gaussian Mixture model* is preferred in the present work [7, Chap.9]. This method estimates the distribution of individuals thanks to a linear combination of several simple Gaussian distributions,

called *components*. Each component represents a single group and is defined by a mean (the center of the group), a covariance matrix (measuring dispersion around the centre) and a mixing coefficient. These three parameters are usually determined through the maximization of the likelihood of the repartition of the individuals between each component ⁴. To do so, the expectation-maximization (EM) algorithm is widely used. Two steps are repeated until convergence: (E) calculation of the conditional expectation of the likelihood function and (M) maximization of this function to determine the components parameters. In addition, Variational Inference [7, Chap. 10] is used in order to avoid the over-partitioning and the emergence of singularities [7, pp 481].

2.4.2 Self-Organizing Maps

Another difficulty when analysing the optimization results is the large number of dimensions of the problem. When it is greater than three, standard plots can no longer be used because it leads to the loss of information [83]. The *Self-Organizing Maps* (SOM), proposed by Kohonen [37], have demonstrated their relevance in analysing the results of large dimension problems [78]. The method is based on an artificial neural network which organizes the individuals and groups them together by similarity so that two neighbour individuals are fairly similar. Data are represented by a set of maps with a constant topology. This set can be read as geographic maps: each map is carrying an information but the same individual is rigorously at the same position on every map.

The neural network is organised according to a square mesh. The number of neurons composing this mesh is of major importance for the results accuracy. If it is smaller than the population size, averaging effect is causing the same neuron to represent several individuals. In contrary, if too many neurons are used, the values of supernumerary ones are obtained through interpolation. So in practice, the number of neurons has to be close to the population size in order to be representative.

The main advantage of SOM is its ability to present all the results at the same time. The analysis is simplified and the interdependence between parameters and objectives can be easily highlighted. The identification of critical parameters is also possible [48].

2.5 Summary of the method

The different tools involved in the present optimization method had been presented. The articulation between them is shown in Fig. 4. Two main steps are considered. The first one builds the Kriging metamodels based on a CFD solver. To do so, latin hypercube sampling (LHS) is used conjointly with an adaptive sampling based on several infill criteria. The second step actually performs the optimization by using the NSGA-II algorithm as motor of optimization and the metamodels as refined fuels. Finally, the results are analysed by using SOM and clustering.

These tools have been implemented in different ways. The NSGA-II algorithm is an in-house C++ software,

⁴It is the same general idea as the one used to determine the Kriging parameters.

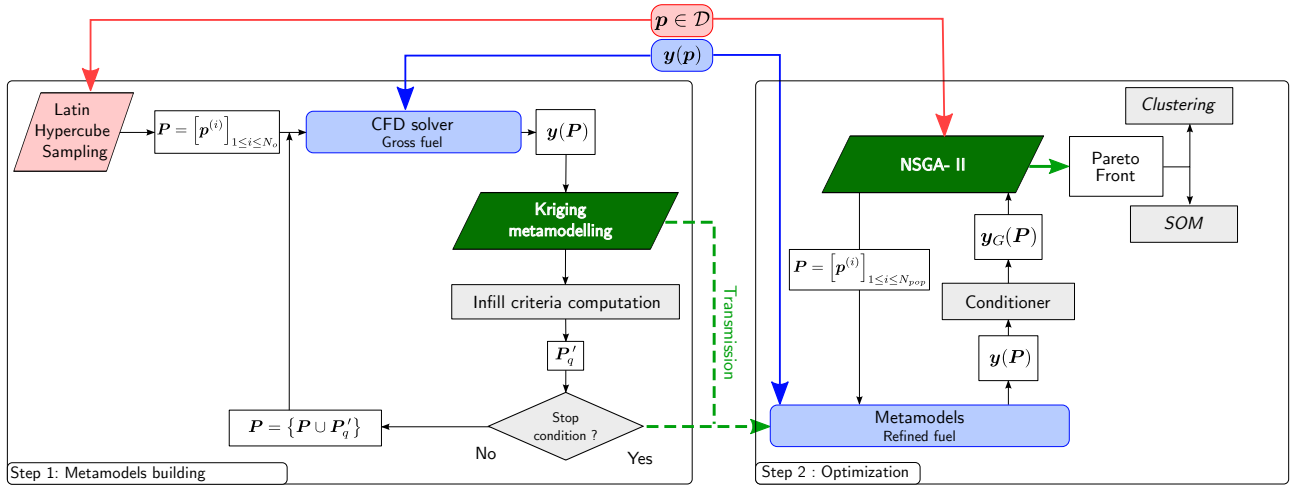


Figure 4: Flow chart of the present optimization method

allowing the use of external fuels thanks to system calls. The sampling and Kriging methods are implemented in R language [64] through several packages: `DiceKriging` and `DiceOptim` for the Kriging [66], `DiceDesign` for the LHS [17] and `GPareto` for the multi-objective infill criteria [6]. The analysis tools had been coded using Python language [23], employing the packages `scikit-learn` for the clustering [60] and `sompy` for the SOM [55].

3. HEAT EXCHANGER MODELLING

This section describes the *air/water cross-flow plate heat exchanger* (CPHX) considered in the present optimization study. It is schematized in Fig. 5. Symmetric *ribs* are periodically placed on each hot channel wall to enhance the heat transfer. A symmetric *diffuser* is used as manifold for the hot side, while the cold side is supposed well distributed. This heat exchanger is intended to be representative of the multi-scale issues highlighted in the introduction.

The effect of the local rib shape and the distribution between each channel are conjointly taken into account in the thermo-hydraulic performances of the heat exchanger.

Thus, the **multi-scale** modelling is based on two different scales: (1) the local one used to analyse the flow **and heat transfer** around the ribs and (2) the global one which gives the heat exchanger performances and takes into account maldistribution issues. For both scales, modelling is based on computational fluid dynamic (CFD) using the *open-source* code `Code_Saturne` version 5.1 [21]. The local scale simulations allow to build two correlations for the Nusselt number and the head losses coefficient based on the ribs shape and flow characteristics. They are then used into the global scale simulation to reproduce the ribs influence on the flow and heat transfer into the active part of the CPHX without meshing them into the channels.

The main characteristics of the heat exchanger as well as the setup of the two scales and the coupling between them is presented in the following.

3.1 Heat exchanger characteristics

The hot stream is air flowing at the mass flow rate \dot{m}_h , temperature $T_{i,h}$ and pressure P_h . The cooling water flows perpendicularly at the mass flow rate \dot{m}_c , temperature $T_{i,c}$ and pressure P_c . The flows characteristics are summarized in Tab. 2.

Table 2: Flows characteristics of the CPHX.

		Hot side: Air	Cold side: Water
Mass flow rate	kg.s ⁻¹	$\dot{m}_h = 0.56$	$\dot{m}_c = 2.86$
Inlet temperature	K	$T_{i,h} = 553.15$	$T_{i,c} = 353.15$
Outlet pressure	Pa	$P_h = 3 \cdot 10^5$	$P_c = 1 \cdot 10^5$

The active part of the CPHX is constituted by a stack of plates forming 13 cold and 12 hot channels of height $H = 0.007$ m, width and length $L_E = W_E = 0.42$ m. The plate thickness is $e_p = 0.001$ m. The total height of the CPHX is thus $H_E = 0.201$ m. The cold channels are smooth while the hot ones are periodically mounted with opposite and staggered trapezoidal ribs, as shown in Fig. 6. Their shape is defined by the height (h_{rib}), base width (E) and top width (e). The angle ψ depends on the three other parameters and it will be used in the results analysis. Two consecutive ribs are spaced with a constant pitch noted by $L = 3H$.

The cold side is assumed to be well distributed, thus the manifold is omitted from Fig. 5 and from the simulation. The manifold of the hot side is composed of three parts. The inlet orifice has a height of $H_{in} = 0.3H_E$ and a length of $L_{in} = 0.5H_{in}$. It is followed by the diffuser which goes from a height of H_{in} to a height of H_E over a length of L_D . The manifold ends with a part of height equal to H_E and a length of $B = 0.3H_E$ connecting the diffuser and the active part.

The ranges of the three local (h_{rib} , e , E) and global (L_D) geometrical parameters is indicated in Sec. 3.2.

3.2 Local scale setup

In order to investigate the influence of the local rib shape, a two-dimensional simulation is carried out. It aims to determine the effect of the rib shape (height h_{rib} , top width e and bas width E) and the Reynolds number on the Nusselt number and the head losses coefficient in order to built the two metamodels. The metamodels construction is discussed in Sec. 4.

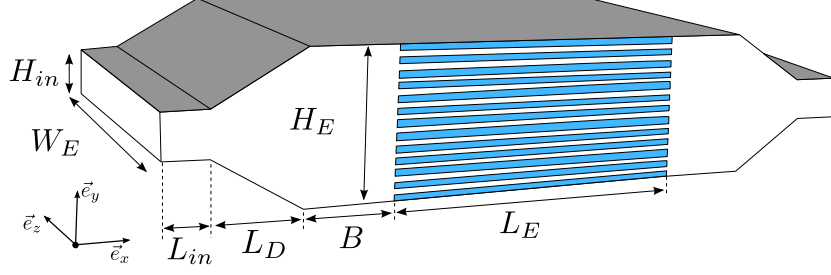


Figure 5: Sketch (not at scale) of the cross-flow plate heat exchanger. The diffuser and the active part are visible. The hot channels are represented in white and the cold ones in blue. W_E , H_E and L_E stand (respectively) for the width, height and length of the active part. H_{in} is the height of the manifold entrance. L_{in} , L_D and B are the length of the different parts of the manifold. The cold side manifold is not considered in the simulation.

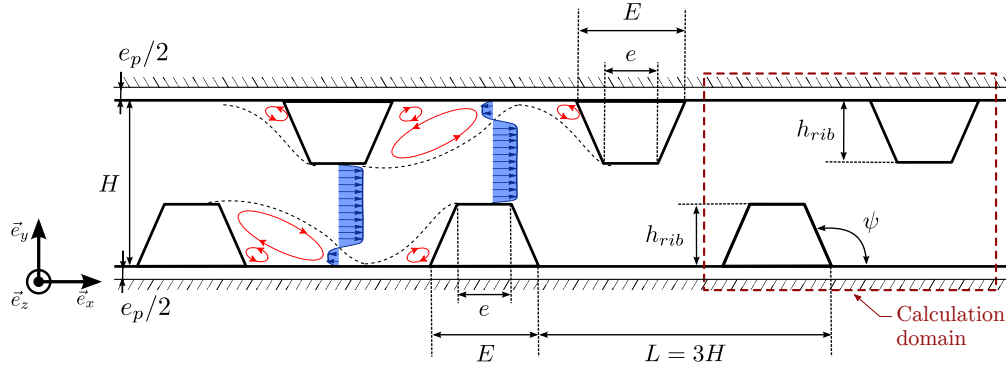


Figure 6: Sketch (not at scale) of the ribs shape, with a naive description of the flow (velocity profiles and recirculation areas). e_p stands for the thickness of the plate. h_{rib} , e and E are the height, top width and base width, respectively. The periodic calculation domain is highlighted by the red dashed line.

3.2.1 Geometry

As the ribs arrangement is periodic, only a single pattern is considered as indicated by the red dashed line in Fig. 6. Both the fluid (air) and solid (steel) domains are taken into account. Indeed, the half thickness ($e_p/2$) of the plate and the ribs form part of the calculation domain. The ribs shape parameters variations, normalized by the canal height, are :

$$L/H = 3 \quad (39)$$

$$e_p/2H = \frac{1}{14} \quad (40)$$

$$h_{rib}/H \in [0.05, 0.3] \quad (41)$$

$$e/2H \in \left[0.05 \frac{L}{4H}, 0.6 \frac{L}{4H} \right] \quad (42)$$

$$E/2H \in \left[0.9 \frac{e}{2H}, 0.7 \frac{L}{4H} \right] \quad (43)$$

The last relation Eqn. (43), used to prevent unmanufacturable shapes, highlights the dependence of the base width lower bound with the top width. However, it is more advantageous from a mathematical point of view to work with independent parameters. Thus, a change of variable is performed to replace E by \tilde{E} , defined as:

$$\tilde{E} = \frac{0.9 \frac{e}{2H} - \frac{E}{2H}}{0.9 \frac{e}{2H} - 0.7 \frac{L}{4H}} \in [0; 1] \quad (44)$$

3.2.2 Flow and physical properties

The flow configuration is modelled by using the incompressible Reynolds Averaged Navier-Stokes (RANS) equations for two-dimensional unsteady air flow and heat transfer.

The Reynolds stresses are modelled using the wall resolved BL- $\overline{v^2}/k$ model [5]. It takes into account the turbulence anisotropy in the wall normal direction through a transport equation for the quantity $\overline{v^2}$, known to be of major influence in heat transfer problems [5, 44]. Thus, this model is recommended for problems with recirculation areas such as ribs. The turbulent heat fluxes are modelled using a simple gradient diffusion hypothesis (SGDH). The turbulent heat fluxes are estimated through a Fourier law based on a turbulent thermal diffusivity and the temperature gradient [16]. The diffusivity is defined as the ratio of the turbulent viscosity and a turbulent Prandtl number set to 1.

The calculation is performed in similarities of Reynolds and Prandtl numbers. Therefore the physical properties are normalized accordingly, and they are assumed independent of temperature variations. The bulk velocity, the density and the heat capacity of the fluid are chosen equal to one. The viscosity and the thermal conductivity are thus derived from the expressions of the Reynolds and Prandtl numbers. The thermal conductivity and density of the solid respect the same ratio compared to the fluid as the real properties. In order to build the correlations with respect to the flow characteristics, the Reynolds number, based on the hydraulic diameter $D_H = 2H$, will vary between 3000 and 13000. Tab. 3 summarizes all this information.

3.2.3 Boundary conditions

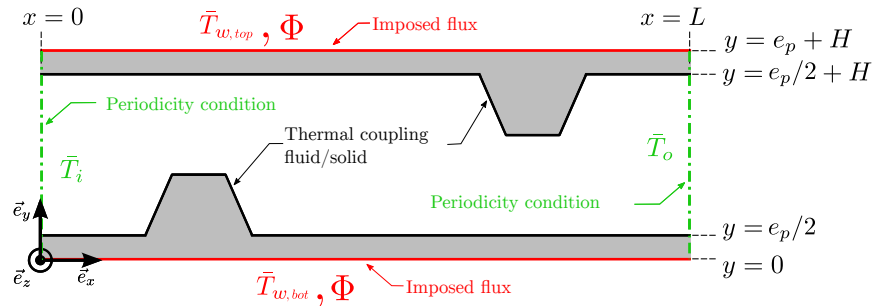


Figure 7: Boundary conditions applied to the local calculation domain. The solid (steel) is in grey and the fluid (air) in white.

The boundary conditions are outlined in Fig. 7. A constant heat flux density ($\varphi = 1 \text{ W.m}^{-2}$) is imposed on

Table 3: Flow characteristic and physical properties.

Quantity	Symbol	Units	Value
Fluid (Air)			
Reynolds number	Re_{DH}	[-]	[3 000; 13 000]
Prandtl number	Pr	[-]	0.7
Bulk velocity	U_{ref}	m.s^{-1}	1
Density	ρ_h	kg.m^{-3}	1
Viscosity	μ_h	Pa.s	$\frac{\rho U_{ref} 2H}{Re_{DH}}$
Specific heat capacity	$c_{p,h}$	$\text{J.kg}^{-1}.\text{K}^{-1}$	1
Thermal conductivity	λ_h	$\text{W.m}^{-1}.\text{K}^{-1}$	$\frac{c_{p,h}\mu_h}{Pr}$
Solid (Steel)			
Density	ρ_s	kg.m^{-3}	1
Specific heat capacity	$c_{p,s}$	$\text{J.kg}^{-1}.\text{K}^{-1}$	$0.48 c_{p,h}$
Thermal conductivity	λ_s	$\text{W.m}^{-1}.\text{K}^{-1}$	$371.3 \lambda_h$

both lower and upper boundaries (red lines). The solid and fluids domains are thermally coupled (black lines). As a periodic pattern is considered, a streamwise (\vec{e}_x) periodicity condition is required (green lines). Because for this configuration the fully developed periodic regime is reached after five patterns only [65] and because the number of ribs in each channel is far greater than five, the periodicity hypothesis is relevant. This condition involves the use of source terms for the pressure and temperature fields in order to take into account the non-periodic evolution of both quantities [59]. Finally, symmetry conditions are applied to each faces in the \vec{e}_z -direction.

As this simulation aims to determine the heat transfer coefficient, either the heat flux or the wall temperature have to be imposed. As the pattern dimension is small enough regarding the heat exchanger length, one can assume the temperature variation is linear. Thus, the heat flux conditions has been chosen.

3.2.4 Numerical settings

Although the simulation aims to reach a steady state, an unsteady temporal scheme is used. The time step is constant and uniform. It is set to $\Delta t = 0.005\text{s}$ to ensure that the Courant-Friedrichs-Lewy (CFL) condition is below 10. The linear systems for the pressure, velocity and turbulent quantities are solved using a Jacobi method. On the

other hand, the linear system related to the temperature is solved with a bi-conjugate gradient stabilized method (Bi-CGStab2) [77]. Indeed, as a consequence of the monolithic coupling the diffusion matrix for the temperature is unsymmetric and this method is well suited to increase the numerical stability. The convective terms for velocity and temperature are discretized by a centered spatial scheme. To increase the numerical stability, the convective terms of the turbulent quantities are discretized by a first order upwind scheme. The pressure-velocity coupling is solved using a SIMPLEC algorithm. The pressure source term is treated implicitly like a force opposed to the flow directly into the momentum equation.

3.2.5 Post processing: Nusselt number and head losses coefficient

The Nusselt number and the head losses coefficient have to be computed from the results of the simulations. As the simulation was carried out in two-dimensions with a unit width in the \vec{e}_z -direction, the surfaces are assimilated to a length or a height. The mean Nusselt number over the pattern is then calculated as:

$$Nu = \frac{\varphi D_H}{\lambda_h \left(\bar{T}_w - \frac{1}{2} (\bar{T}_i + \bar{T}_o) \right)} \quad (45)$$

with φ the imposed heat flux density, \bar{T}_w the mean surface temperature evaluated on the external walls (see red lines in Fig. 7) and calculated as:

$$\bar{T}_w = \frac{\bar{T}_{w,bot} + \bar{T}_{w,top}}{2} \quad (46)$$

$$= \frac{1}{2L} \int_0^L [T_w(x, y = 0) + T_w(x, y = e_p + H)] dx \quad (47)$$

\bar{T}_i and \bar{T}_o are the mean bulk temperature at the inlet and outlet of the pattern (green lines Fig. 7), calculated as:

$$\bar{T}_i = \frac{\int_{e_p/2}^{e_p/2+H} \rho_h u_x(x=0, y) T(x=0, y) dy}{\int_{e_p/2}^{e_p/2+H} \rho_h u_x(x=0, y) dy} \quad (48)$$

$$\bar{T}_o = \frac{\int_{e_p/2}^{e_p/2+H} \rho_h u_x(x=L, y) T(x=L, y) dy}{\int_{e_p/2}^{e_p/2+H} \rho_h u_x(x=L, y) dy} \quad (49)$$

Note that, as the temperature difference in Eqn. (45) is calculated between the solid boundaries and the bulk flow, the obtained Nusselt number takes into account the conductive contribution of the solid.

The head losses coefficient is calculated as:

$$C_f = \frac{\Delta P_{i,o}}{0.5 \rho_h U_{ref}^2} \frac{D_H}{L} \quad (50)$$

where $\Delta P_{i,o}$ is the pressure variation between the inlet and outlet of the pattern and U_{ref} is the bulk velocity calculated as:

$$U_{ref} = \frac{1}{H} \int_{e_p/2}^{e_p/2+H} u_x(x=0, y) dy \quad (51)$$

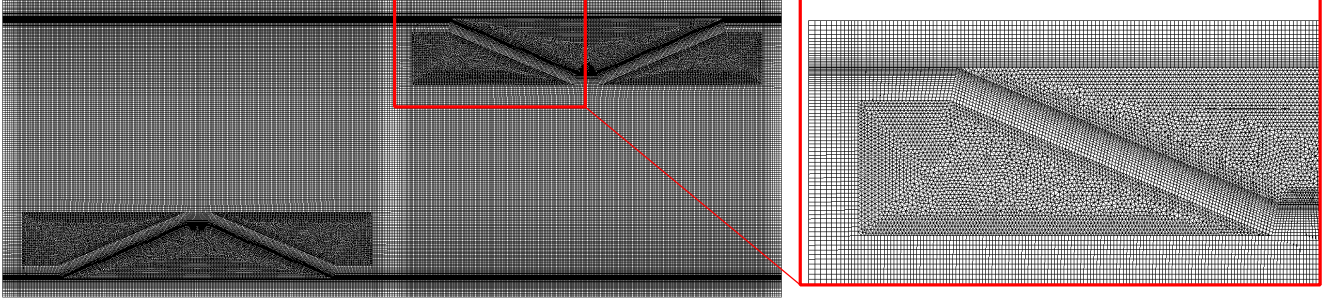


Figure 8: Rib mesh illustration.

The Nusselt number is normalized by Nu_0 , extracted from the Dittus-Boelter correlation [3, pp. 544]:

$$Nu_0 = 0.023Re_{D_H}^{0.8}Pr^{1/3} \quad (52)$$

and the head losses coefficient by C_{f0} , extracted from the Blasius correlation [82, pp. 307]:

$$C_{f0} = 0.3164Re_{D_H}^{-0.25} \quad (53)$$

3.2.6 Mesh

The mesh is unstructured with about 150 000 cells mixing hexahedral and prismatic elements as shown in Fig. 8. A boundary layer mesh is used to satisfy the $y^+ \leq 1$ condition for the first fluid cell near the wall, required by the turbulence model. The prisms are located in high deformation areas due to the change of the ribs shape parameters. In order to modify the ribs shape during the correlations construction process, a parametrized geometry and an automatic meshing strategy have been employed. The ANSYS[®] Design Modeler and Meshing⁵ tools have been used to do so.

Obviously, carrying out mesh sensitivity studies for all the shapes explored during this process is not feasible due to the amount of possible combinations. Thus one mesh sensitivity analysis was performed to validate the meshing strategy used for all the shapes. As near wall phenomena are of major influence in this case, particular attention has been paid to the mesh structure in this area. The maximal value of y^+ has been used as indicator of the quality, verifying that it remains below 2.

Verification and validation of this configuration exists in the literature. The same solver and mesh density as Keshmiri *et al.* [34] is used in the present paper.

⁵Version 18.3

3.3 Global scale setup

The global scale is investigated through a three-dimensional simulation, in order to capture distribution and thermal phenomena, and the coupling between both. The present multi-scale modelling is inspired by a well-known porous approach [53, 56]. However in the present work, in contrast to other previous works using non specific experimental correlations, the head losses and thermal coefficient are based on the numerical correlations from the local scale.

3.3.1 Geometry and mesh

The main features of the geometry have been already presented in Sec. 3.1 and Fig. 5. A symmetry plane is assumed in the \vec{e}_y direction to limit the simulation to the half of the heat exchanger, *i.e.* six hot channels and six and half cold ones. The diffuser length may vary in the range:

$$L_D/H_{in} = [2; 5] \quad (54)$$

The hot side, the solid plates and the cold side are taken into account and simulated.

The multi-scale approach required a specific mesh, shown in Fig. 10. Indeed, the ribs are not meshed in each channel and their impact on the thermo-hydraulic behaviour is modelled by the correlations of the Nusselt number and the head losses coefficient. However, they are based on bulk quantities (velocity and temperature) as expressed in Eqs. (45) and (50). **To be consistent with the information given by them**, only one cell in the height of the channel is used to discretize it. Thus the quantities at the cell center are representative of the bulk behaviour. The distribution part is visible on the left side of Fig. 10. The mesh is formed by hexahedral cells and a boundary layer mesh is used near the walls. The active part is also constituted by a majority of hexahedral cells. **As these two parts form a unique computational domain, and** to avoid a mesh quality degradation, a transitional area composed by prisms is used, as shown in Fig. 10. **Finally, the steel plates are meshed with hexahedral cells, using three elements in the thickness.**

A mesh sensitivity study has been carried out for a diffuser length equal to $L_D = 3.5H_{in}$ in order to evaluate the mesh influence on the mass flow distribution between each channel. The quantity of interest is the absolute mass flow difference on each channel regarding the finer mesh :

$$\epsilon_{i,j} = \frac{|\dot{m}_{i,j} - \dot{m}_{8,j}|}{\dot{m}_{8,j}} \quad (55)$$

with $i \in [1, 8]$ the number of mesh and $j \in [1, 6]$ the number of channels. also the maximum value of y^+ is also analysed. **The results are shown on Fig. 9.** A mesh with 3 700 000 cells was found sufficient to see an insignificant variation of the mass flow distribution with respect to the finer mesh used (7 000 000 cells). **The y_{max}^+ value is close to 3 a sufficiently low value to ensure a good prediction of the near-wall flow by the turbulence model.**

The meshing strategy for this configuration is not robust enough to automatize the meshing procedure. Moreover, the computational time is important for this large mesh. Additionally, restarting the calculation on the same mesh

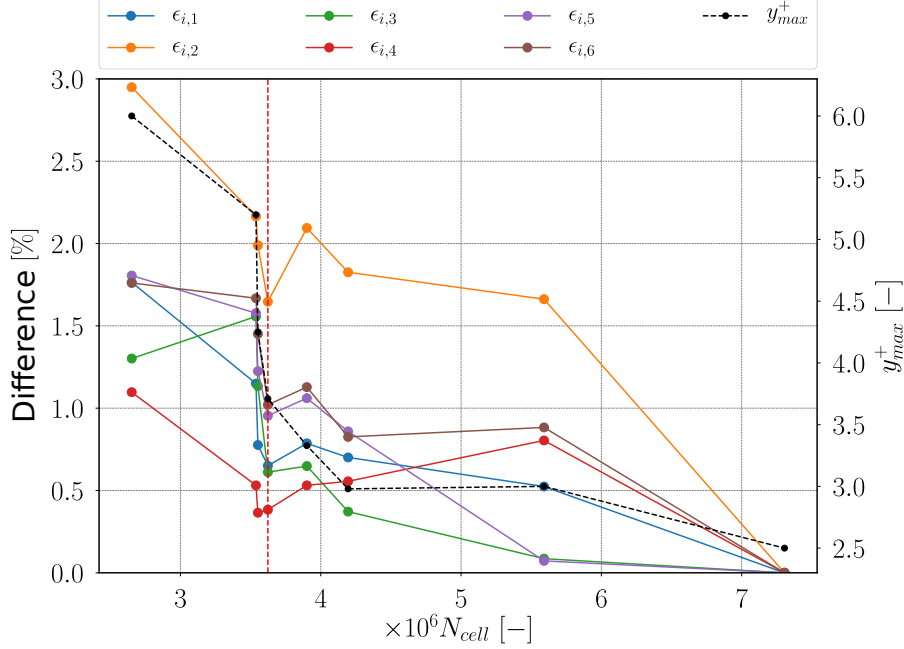


Figure 9: Mesh sensitivity analysis. The $\epsilon_{i,j}$ evolution is reported on the left axis (coloured lines) and the y_{max}^+ on the right axis (dashed black line) respect to the number of cells. The red dashed line indicates the selected mesh.

is also a necessary issue for efficiency purpose. Therefore, to be able to investigate the different diffuser lengths L_D , a mesh morphing method based on radial basis functions (RBF) is employed since it produces high quality deformed mesh suitable for CFD applications [2, 47]. Knowing the displacement of a set of control points, the method propagates this displacement to the rest of the mesh, without requiring any mesh connectivity information. The control points are located at the boundaries of the mesh. Thus, the variation of the diffuser length causes a displacement of the control points and a corresponding deformation of the mesh.

3.3.2 Flow and physical properties

The configuration is modelled by the incompressible RANS equations. **The energy equation is solved in both fluid and solid domains in the three conditions.** The Reynolds stresses are modelled by the $k-\omega$ SST model [50]. Indeed the study of El-Behery and Hamed [18] has shown that the model is able to estimate the diffuser recirculation appropriately, also showing numerical robustness. The physical properties are assumed independent of temperature variations. They are taken at temperature $T_{i,h}$ and pressure P_h for the hot air and $T_{i,c}$ and P_c for the cold water. The properties of stainless steel are used for the solid plates. However, as the local scale Nusselt number takes into account the conductivity in half of the plate thickness, the thermal conductivity is multiplied by two to comply the global thermal resistance. To reinforce the numerical stability of the simulation, the density of the cold water and the solid are set equal to the air density. As a steady state is pursued, this modification is not influencing the

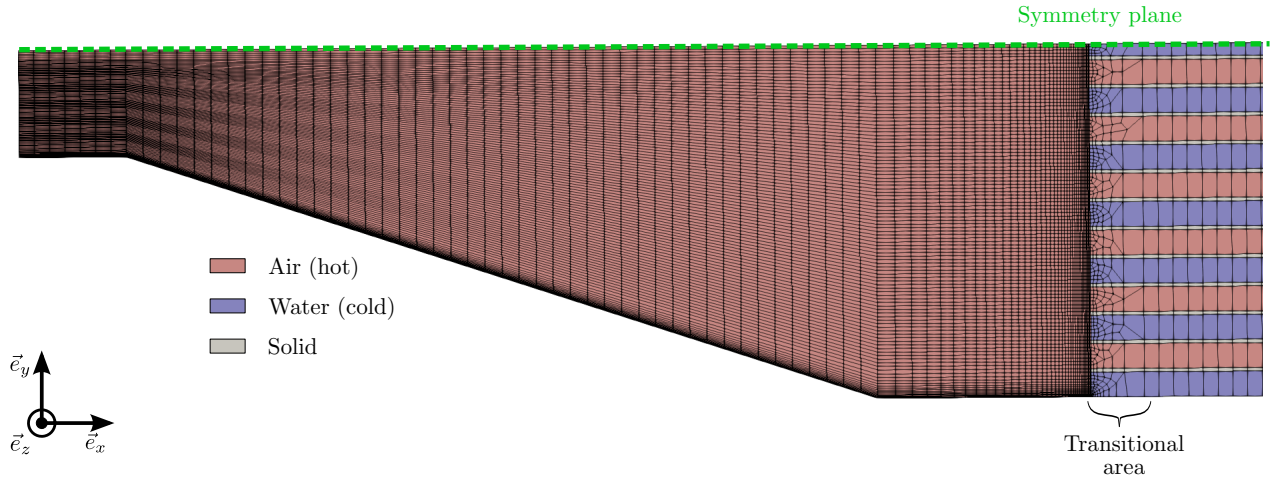


Figure 10: Global scale mesh at the inlet. Hot channels are represent in red and cold one are represented in blue.

thermal behaviour of the heat exchanger. The velocity of the water at the inlet is adjusted to meet the required mass flow and Reynolds number. The properties values are presented in the Tab. 4, expressed with respect to the hot fluid properties.

3.3.3 Boundary and volume conditions

The boundary conditions are highlighted in Fig. 11. Only half heat exchanger is considered and a symmetry condition (in green) is used. An inlet air mass flow rate equal to $\dot{m}_h = 0.262 \text{ kg.s}^{-1}$ at temperature $T_{i,h} = 553.15 \text{ K}$ is imposed on the hot side. A similar condition is applied for the cold side with a water mass flow rate equal to $\dot{m}_c = 1.43 \text{ kg.s}^{-1}$ at temperature $T_{i,c} = 353.15 \text{ K}$. At the outlets, zero Neumann condition for the velocity and the temperature is applied, whereas a pressure of $P_h = 3 \cdot 10^5 \text{ Pa}$ is imposed on the hot side and $P_c = 1 \cdot 10^5 \text{ Pa}$ on the cold one.

The interface between the fluids domain and the solid domain allows a thermal coupling between them (orange lines on Fig. 11). The heat exchange coefficient which is generally computed from the flow conditions is overwritten using the Nusselt number correlation computed from the local scale for the hot side **For each channels, the Reynolds number is evaluated at the middle (fully developed flow). The rib shape being imposed, the Nusselt number is thus computed using the local metamodel ($Nu = f(Re_{D_H}, \mathbf{p})$). The convective heat transfer coefficient is calculated and imposed at the face interface into the code. The code uses this value to compute the flux at the interface. Finally, the heat coefficient is varying for each channel but is constant into the channel. The same method is used for the cold side, but using the Gnielinski correlation to determine the Nusselt number [3, pp. 545].**

The other walls (grey and black) are adiabatic.

The head losses in the active part are computed using an additional source term for the pressure gradient:

$$\vec{\nabla} P = -\frac{1}{2} \rho_h \frac{C_f}{D_H} |\vec{u}| \vec{u} \quad (56)$$

Table 4: Physical properties for the global scale simulation.

Quantity	Symbol	Units	Value
Hot air at 553.15 K and $3 \cdot 10^5$ Pa			
Density	ρ_h	kg.m ⁻³	1.89
Viscosity	μ_h	Pa.s	$2.9 \cdot 10^{-5}$
Specific heat capacity	$c_{p,h}$	J.kg ⁻¹ .K ⁻¹	1077
Prandtl number	Pr	[-]	0.7
Thermal conductivity	λ_h	W.m ⁻¹ .K ⁻¹	$c_{p,h}\mu_h/Pr = 0.045$
Cold water at 353.15 K and $1 \cdot 10^5$ Pa			
Density	ρ_c	kg.m ⁻³	ρ_h
Viscosity	μ_c	Pa.s	$30\mu_h$
Specific heat capacity	$c_{p,c}$	J.kg ⁻¹ .K ⁻¹	$4 c_{p,h}$
Thermal conductivity	λ_c	W.m ⁻¹ .K ⁻¹	$14 \lambda_h$
Stainless steel			
Density	ρ_s	kg.m ⁻³	ρ_h
Specific heat capacity	$c_{p,s}$	J.kg ⁻¹ .K ⁻¹	$0.48 c_{p,h}$
Thermal conductivity	λ_s	W.m ⁻¹ .K ⁻¹	$742 \lambda_h$

where \vec{u} is the velocity vector and $|\vec{u}|$ is its magnitude, C_f is the head losses coefficient, ρ_h is the density and $D_H = 2H$ is the hydraulic diameter. The head losses coefficient is obtained from the local scale correlation for the hot side and from the Pethukhov correlation [3, pp. 522] for the cold side.

3.3.4 Numerical parameters and coupling implementation

Even if a steady solution is sought, a time marching scheme is used to ensure the simulation stability. The time step is constant and uniform, with a value of $\Delta t = 0.0004$ s ensuring that the CFL and Fourier numbers remain below 10. The number of time steps is fixed to 80 000 to reach the steady state. The linear solvers employed are the same as presented in Sec. 3.2.4, as well as the gradient calculation method and the pressure-velocity coupling algorithm. All the convective terms are discretized by means of a first order upwind scheme.

As the mesh is large, all the simulation are performed using restart from a previous converged solution. The correlations for the Nusselt number and the head losses coefficient are built using Kriging metamodels. During the simulation, a communication step is added to extract the information from the metamodels. At each time step, the

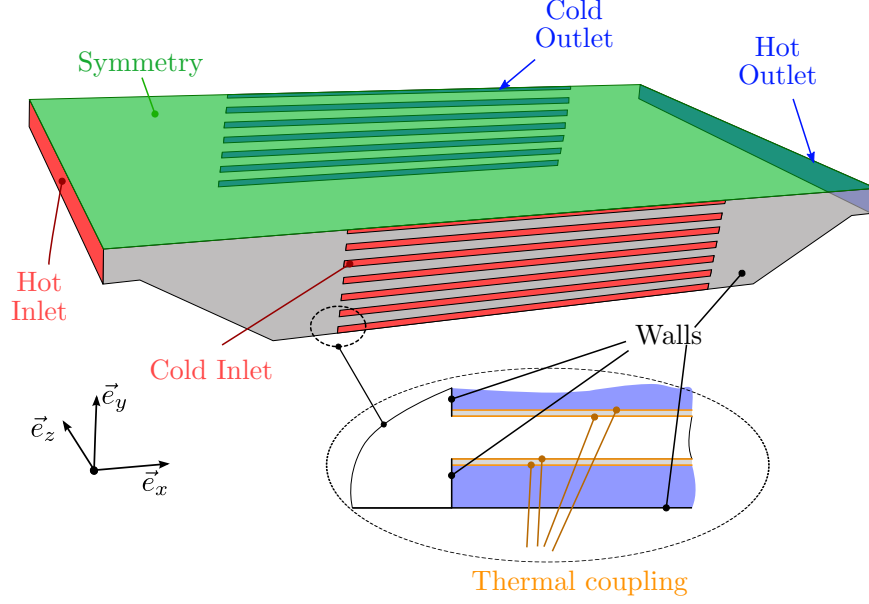


Figure 11: Boundary conditions applied to the global calculation domain. The surrounded details highlight the conditions at the fluid/solid interface and at the distribution/active limits.

Reynolds number in every channel is computed, sent to the metamodels which give back the coefficient values. They are used to overwrite the heat exchange coefficient at the coupled interface and to compute the pressure gradient source term following Eqn. (56).

3.3.5 Performances post-processing

The CPHX performances are expressed through the effectiveness ε and the pressure drop ΔP . The distribution standard deviation of the mass flow between channels Υ is also an interesting quantity to measure the influence of the manifold.

The effectiveness is the ratio between the actual heat transfer rate and the maximum heat transfer rate:

$$\varepsilon = \frac{\Phi}{\Phi_{max}} \quad (57)$$

with the maximal heat transfer rate:

$$\Phi_{max} = \min(\dot{m}_h c_{p,h}, \dot{m}_c c_{p,c}) (\bar{T}_{i,h} - \bar{T}_{i,c}) \quad (58)$$

and the heat transfer rate computed at the hot side:

$$\Phi = \dot{m}_h c_{p,h} (\bar{T}_{o,h} - \bar{T}_{i,h}) \quad (59)$$

where $\bar{T}_{i,h}$ and $\bar{T}_{i,c}$ are the mean bulk inlet temperature of the hot and cold side and $\bar{T}_{o,h}$ is the mean bulk outlet

temperature of the hot side. These temperatures are computed through an oriented surface S as:

$$\bar{T} = \frac{\int_S \rho \vec{u} T \cdot d\vec{S}}{\int_S \rho \vec{u} \cdot d\vec{S}} \quad (60)$$

The pressure drop is calculated as the total pressure difference between the inlet (i) and the outlet (o):

$$\Delta P = (\bar{P}_i - \bar{P}_o) + \frac{1}{2} \left(\frac{\int_{S_i} \rho |\vec{u}| \vec{u} \cdot d\vec{S}_i}{S_i} + \frac{\int_{S_o} \rho |\vec{u}| \vec{u} \cdot d\vec{S}_o}{S_o} \right) \quad (61)$$

where S_i and S_o are the inlet and outlet surfaces with their corresponding normals pointing out of the domain.

The distribution standard deviation for the hot side is calculated as [70, 38]:

$$\Upsilon = \sqrt{\frac{1}{N_{ch,h}} \sum_{k=1}^{N_{ch,h}} \left(\dot{m}_{h,k} - \frac{\dot{m}_h}{N_{ch,h}} \right)^2} \quad (62)$$

where $N_{ch,h}$ is the number of hot channels, $\dot{m}_{h,k}$ is the mass flowing into the k -th channel and \dot{m}_h is the total mass flow on the hot side.

4. LOCAL SCALE CORRELATIONS

As previously said, the local scale simulations aim to build correlations of the thermo-hydraulic behaviour inside the active part for different rib shapes (h_{rib}/H , $e/2H$, \tilde{E}) and flow conditions (Re_{D_H}). These correlations are based on Kriging metamodells. The problem is stated as a minimization one. Therefore, the performances are expressed as $-Nu/Nu_0$ and C_f/C_{f0} .

4.1 Adaptive sampling

In order to build cheap and accurate metamodells, the adaptive sampling strategy presented in Fig. 12 is used. The two infill criteria are the MMSE and the q-EI. The former, which allows exploration of the objective space, is particularly interesting when metamodells are used as correlations as it increases the prediction accuracy over the whole space. For its part, the q-EI criterion adds observations in the probable optimum neighbourhood. **Indeed, in order to ensure robustness of the optimization process the optimum neighbour area of each objective have to be explored. This will lead to a better description of the final Pareto front.**

The initial design of experiments \mathbf{P} is obtained through an optimized LHS [12] based on 40 observations. Then, the two DOE are infilled independently of each other **in order to avoid numerical instability caused by over-sampling** [48]. The observations are evaluated by the simulation setting up as described in Sec. 3.2. Next, the performances are post-processed and the two metamodells are built. At this point, the two infill criteria are computed and at each iteration, 6 observations are provided, 2 by the MMSE criteria (noted \mathbf{P}'_2) and 4 by the q-EI (noted \mathbf{P}'_4). The stop conditions are defined by Eqs. (37) and (38) with the tolerance set to $\delta_{q-EI} = 0.1\%$ and $\delta_{MMSE} = 3\%$, respectively.

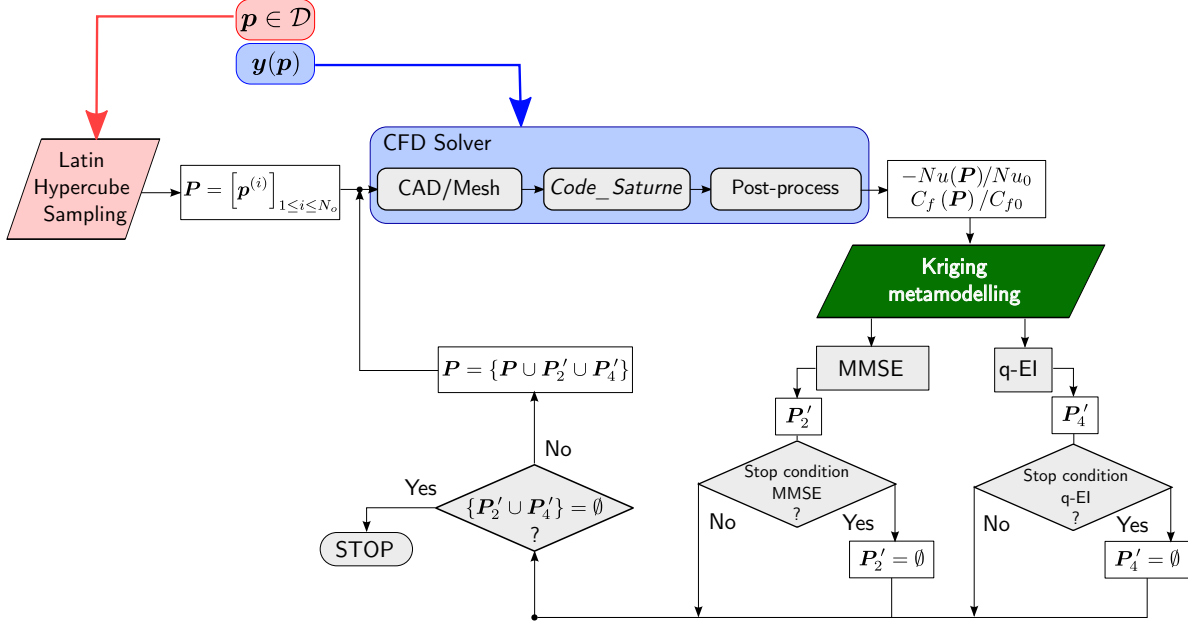


Figure 12: Adaptive sampling flowchart for the correlations building.

These values are similar to those usually chosen in the literature [69]. If the value provided by the criterion is below the tolerance, no observation is added. If both criteria give an empty set of observations, the sampling is finished. Otherwise, the observations are added to the DOE and a new metamodel is built.

4.2 Metamodels settings

The *Matérn* $\nu = 5/2$ function is used as mono-dimensional covariance function in Eqn. (7), to stabilize the estimation of the Kriging parameters. It is expressed as:

$$\tilde{R}(p^{(1)} - p^{(2)}, \theta) = \left(1 + \frac{\sqrt{5}|p^{(1)} - p^{(2)}|}{\theta} + \frac{5(p^{(1)} - p^{(2)})^2}{3\theta^2} \right) \exp\left(-\frac{\sqrt{5}|p^{(1)} - p^{(2)}|}{\theta}\right) \quad (63)$$

The trend $v(\cdot)$ in Eqn. (5) is set as an unknown constant. A nugget effect is added to avoid potential perturbation in the simulations response. The minimization of the opposite log-likelihood function is based on the GENOUD algorithm [49].

4.3 Metamodels analysis

Fig. 13 shows the evolution of the infill criteria values (see Eqs. (37) and (38)) and the number of observations in each DOE during the sampling. The Nusselt number metamodel is built using 62 observations, while the head losses coefficient one is built using 138. For both performances, the MMSE value decreases monotonously until it reaches the tolerance at the eighth iteration. That indicates the end of the sampling process for the Nusselt number. On

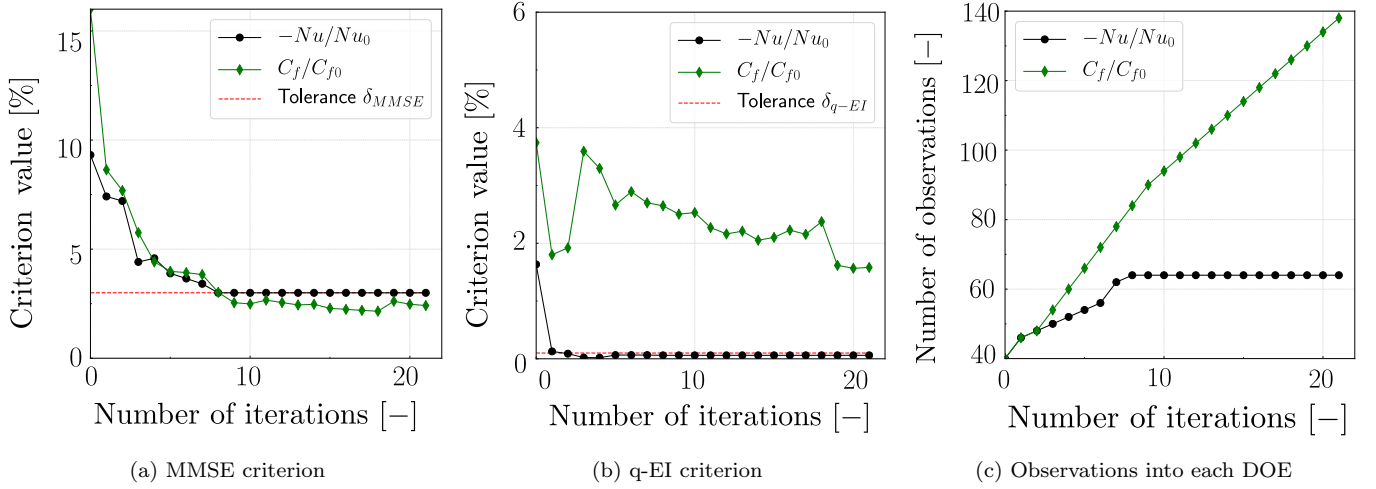


Figure 13: Criteria and number of observations evolution respect to the number of sampling iterations. Nusselt number information are in black, head losses coefficient one in green. The red dashed line figures the tolerance.

the other hand, the evolution of the q-EI values is quite different. The tolerance is rapidly reached for the Nusselt number. For the head losses coefficient, the decrease of the criteria value is slow and the tolerance is never achieved. Therefore, the sampling was arbitrary stopped at the 22nd iteration, the benefit in terms of criterion value being not significant during the three last iterations. The evolution of the number of observations in each metamodel highlights the end of the sampling for the Nusselt number after 8 iterations (Fig. 13(c)). The change of trend of the ratio C_f/C_{f0} is due to the MMSE infill stop ($\mathbf{P}'_2 = \emptyset$).

By analysing the Kriging mean response surface of the two metamodels, the q-EI criteria behaviour may be explained. Fig. 14 shows the contour plot of both performances at $Re_{D_H} = 8000$ and $\tilde{\mathbf{E}} = \mathbf{0}$. The minimum area (in blue) for the value $-Nu/Nu_0$ is limited. Moreover, the gradient values are large in its surrounding and the variation is monotonous. Thus, the q-EI criterion easily locates this area and the sampling process is fast. In contrary, the minimum area for C_f/C_{f0} is broader with small gradients. Therefore, at each iteration, the q-EI criterion keeps finding new observations which are probably close to the minimum. **This is clearly highlighted by the position of the observations, marked by the black points on Fig. 14(b). Indeed, almost 70% of the observations added during the last 12 iterations are located in the minimum area of the head losses coefficient.** One can reasonably says that the stop condition will be reached when the entire area will be sampled. However, increasing the number of observations may degrade the metamodels accuracy **due to over-sampling [48]**. This effect is visible in Fig. 13(a): the MMSE criterion value increases for C_f/C_{f0} during the last three iterations.

To verify the metamodels accuracy, a cross-validation [17] has been performed. The relative quality indicators (RMSE) are below 2% for both metamodels. Moreover, the variation of the characteristic length-scale and trend values resulting of the validation process are negligible. Several trends has been investigated *a posteriori*, without

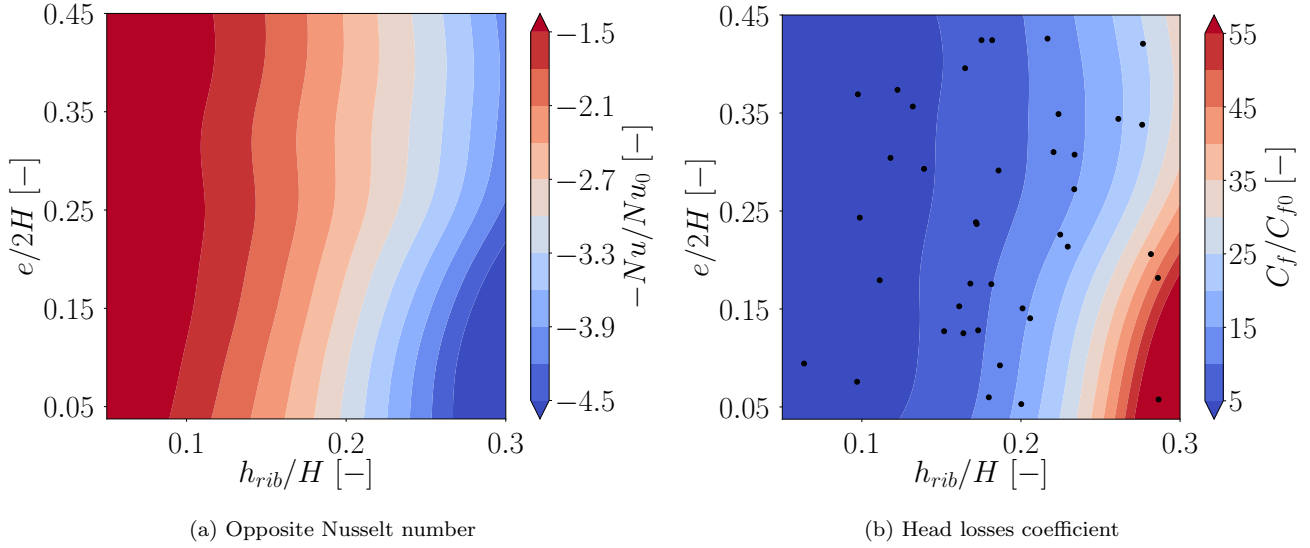
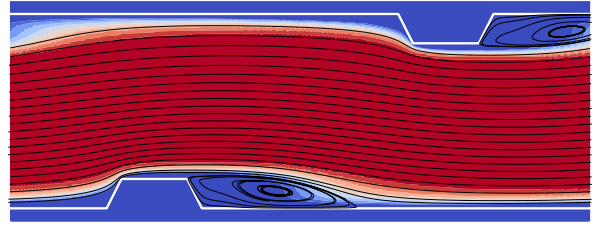
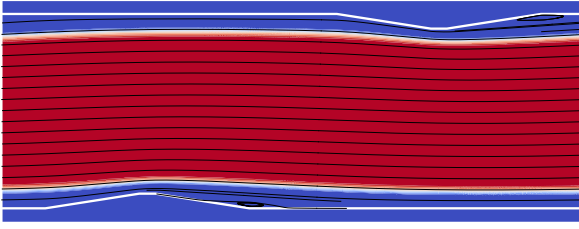


Figure 14: Performances contour plot at $Re_{D_H} = 8000$ and $\tilde{E} = 0$. Nusselt number is on the left (a) and head losses coefficient on the right (b). The points highlight the observation added by the q-EI during the last 12 iterations. The minimum area (in blue) is broader for the head losses coefficient.

significant improvements of the metamodels accuracy. Finally, the nugget effect influence is analysed by checking the value of the estimated additional variance τ^2 . For both metamodels, the τ^2 value is around $10^{-6}\%$ of the performances ranges. Thus, the impact of adding nugget effect on the metamodels approximation is negligible. However, the nugget effect improves the robustness of the method, allowing an other degree of freedom to build the interpolation.

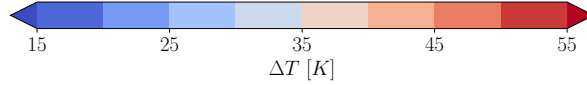
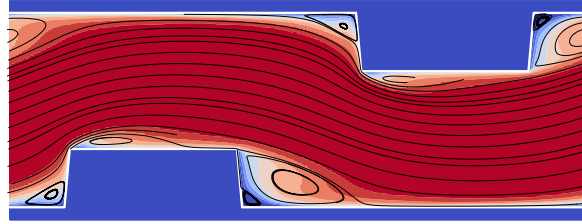
4.4 Flow analysis and correlations check-out

The Fig. 15 shows the temperature difference contours and the streamlines of three different ribs shape of the DOE. The Reynolds number describing to the flow is $Re_{D_H} = 8000$. The shapes are representative of the ribs effect on the flow. The shape on Fig. 15(a) is characterized by a small height and an important base width (\tilde{E}). The rib pattern is then slightly different of a flat plate. The flow highlighted by the streamlines is also similar as the flat plate one. Only small flow recirculation is visible downstream the ribs. The temperature is stratified, and the heat transfer rate is low. This shape leads to a low heat losses coefficient and low Nusselt Number. The shape on Fig. 15(b) is characterized by a medium height and widths. These trapezoidal rib leads to a more important flow recirculation downstream. This increase the fluid mixing and therefore the heat transfer rate. Finally, the rib on Fig. 15(c) is characterized by a maximal height ($h_{rib}/H = 0.3$) and important width. The flow blockage is in this case important, leading to an important flow mixing and heat transfer rate. The sharp angle of the rib at leading edge causes a recirculation upstream. Also a recirculation on the top of the rib is highlighted by the streamlines. This is due to



(a) $h_{rib}/H = 0.0755$, $e/2H = 0.0414$, $\tilde{E} = 1$, $Re_{DH} = 8000$

(b) $h_{rib}/H = 0.151$, $e/2H = 0.1691$, $\tilde{E} = 0.213$, $Re_{DH} = 8000$



(c) $h_{rib}/H = 0.3$, $e/2H = 0.43$, $\tilde{E} = 0.22$, $Re_{DH} = 8000$

Figure 15: Contour of the difference of temperature (respect to the wall temperature) and streamlines for three different ribs shape of the DOE.

the important blockage ratio [65]. This shape leads to an important head losses coefficient and important Nusselt number.

Fig. 16 shows the evolution of the normalized Nusselt number (Nu/Nu_0) and normalized head losses coefficient (C_f/C_{f0}) for two different ribs shapes over the Reynolds number range. As the Reynolds number increases, the relative heat transfer rate decreases whilst the relative head losses coefficient increases. Thus, for large Reynolds number, using ribs instead of a smooth channel is less beneficial in terms of thermo-hydraulics performances. For significant height, the flow blockage is more important. Thus the recirculation areas are more noticeable and lead to an increase of Nu/Nu_0 and C_f/C_{f0} . The observed behaviours are similar to those presented in previous studies [27, 81], allowing the validation of the physical meaning of the built correlations.

5. MULTI-SCALE OPTIMIZATION

As mentioned in the introduction, most of the studies of the literature are focussed on either the local scale or the global scale. However, the fact of considering both scales in the same optimization process is relevant regarding the

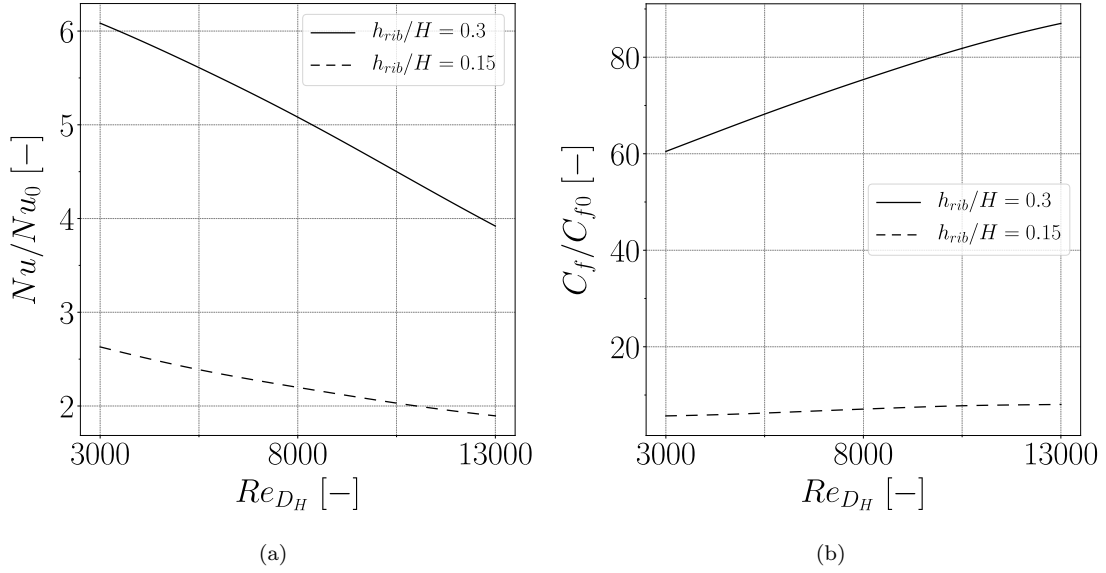


Figure 16: Normalized Nusselt number (a) and normalized head losses coefficient (b) against Reynolds number for ribs height equal to $h_{rib}/H = 0.3$ (solid line) and $h_{rib}/H = 0.15$ (dashed line) keeping constant the other parameters ($e/2H = 0.05$ et $\psi = 90$ deg).

paramount influence of the maldistribution issues on the heat exchanger performances.

5.1 Optimization problem statement

The multi-objective shape optimization of the CPHX performances is addressed in the current section. The scale coupling is taken into account by using the local ribs shape parameters (h_{rib}/H , $e/2H$ and \tilde{E}) and the diffuser length (L_D) as parameters for the optimization. The hot and cold mass flows are kept constant as reported in Sec. 3.3.3 Thus, the minimization problem is expressed as:

$$\left\{ \begin{array}{ll} \min_{\mathbf{p} \in \mathbb{R}^4} & -\varepsilon(\mathbf{p}) & (64) \\ \min_{\mathbf{p} \in \mathbb{R}^4} & \Delta P_{ech}(\mathbf{p}) & (65) \\ \text{subject to} & h_{rib}/H \in [0.05, 0.3] & (66) \\ & e/2H \in [0.0375; 0.45] & (67) \\ & \tilde{E} \in [0; 1] & (68) \\ & L_D/H_{in} \in [2; 5] & (69) \end{array} \right.$$

with the vector of parameters $\mathbf{p} = (h_{rib}, e, \tilde{E}, L_D) \in \mathbb{R}^4$. The effectiveness ε is given by the Eqn. (57). The pressure drop objective ΔP_{ech} is calculated as the sum of the hot side pressure drop ΔP_h , depending on \mathbf{p} and the constant

- IMSE criterion allows for exploration of the parameter space and increases the global accuracy of the approximation, which is useful to avoid local optima.

This step starts by creating a coarse DOE \mathbf{P} through an optimized LHS of 37 observations. At each iteration, 4 observations (\mathbf{P}'_4) are added to the DOE: two by IMSE⁶, one by EHI and one by EEV. The enrichment of the DOE is limited by a maximal number of simulations initially set to 80.

To setup the method, the *Matérn* $\nu = 5/2$ function is used as mono-dimensional covariance function as it stabilizes the estimation of the Kriging parameters. The trend $v(\cdot)$ is treated as an unknown constant. The nugget effect is not applied as the number of observations in the DOE is not large enough. The GENOUD algorithm is used to minimize the opposite log-likelihood function and to determine the Kriging parameters.

5.2.2 Metamodelling convergence and analysis

The information computed by the infill criteria is not appropriate to analyse the convergence of the adaptive sampling. Thus, the hypervolume is used as indicator. When the hypervolume calculated thanks to the DOE observations is stable, the Pareto front is assumed to be well described and the metamodels approximations are accurate [61]. Fig. 18(a) shows the evolution of the indicator during the sampling. After an increase of the hypervolume, a stable value is reached for the iterations 7 to 9. At the tenth iteration, the value increase again. This is due to the discovery of a new part of the Pareto front by the infill criteria. When the sampling stop after 12 iterations, the asymptotic behaviour is not reached. To confirm this trend, more iterations would be necessary, but they have not been done in order to reflect the industrial constraints limitatiing the total number of CFD computations to 80.

Fig. 18(b) shows the 76 observations according to the criterion that added it in the objective space . The crosses (+) mark the non-dominated observations of the DOE. The initial observations (\square) obtained through LHS provide a space filling of the parameter space leading to a proper distribution of the observations in the objective space. It can be noticed that the objective space seems to be tight: for the same ΔP_{ech} the effectiveness variation is small. The IMSE criterion (\circ) leads to a good spreading of the observations, due to its intrinsic exploratory nature. This criterion tends also to fill in the gaps, as shown for $-\varepsilon < -0.5$. The two exploitation criteria highlight different behaviour. The observations obtained through EHI (\diamond) are concentrated around $-\varepsilon = -0.28$ and $\Delta P_{ech} = 250$ Pa. On the contrary, the observations given by the EEV (\diamond) are distributed along the front. This behaviour is due to the objective scale difference. The EEV criteria formulation make it independent of this difference while the EHI definition is highly impacted by this scale difference because it is based on the hypervolume measure [20]. Therefore, as $\Delta P_{ech} \propto 1000\varepsilon$, the criterion favours the area with low pressure drop, leading to the best expected improvement as shown by large gradient area in Fig. 18(c). The observation added by the EEV criteria at $-\varepsilon = -0.53$

⁶One for each objective

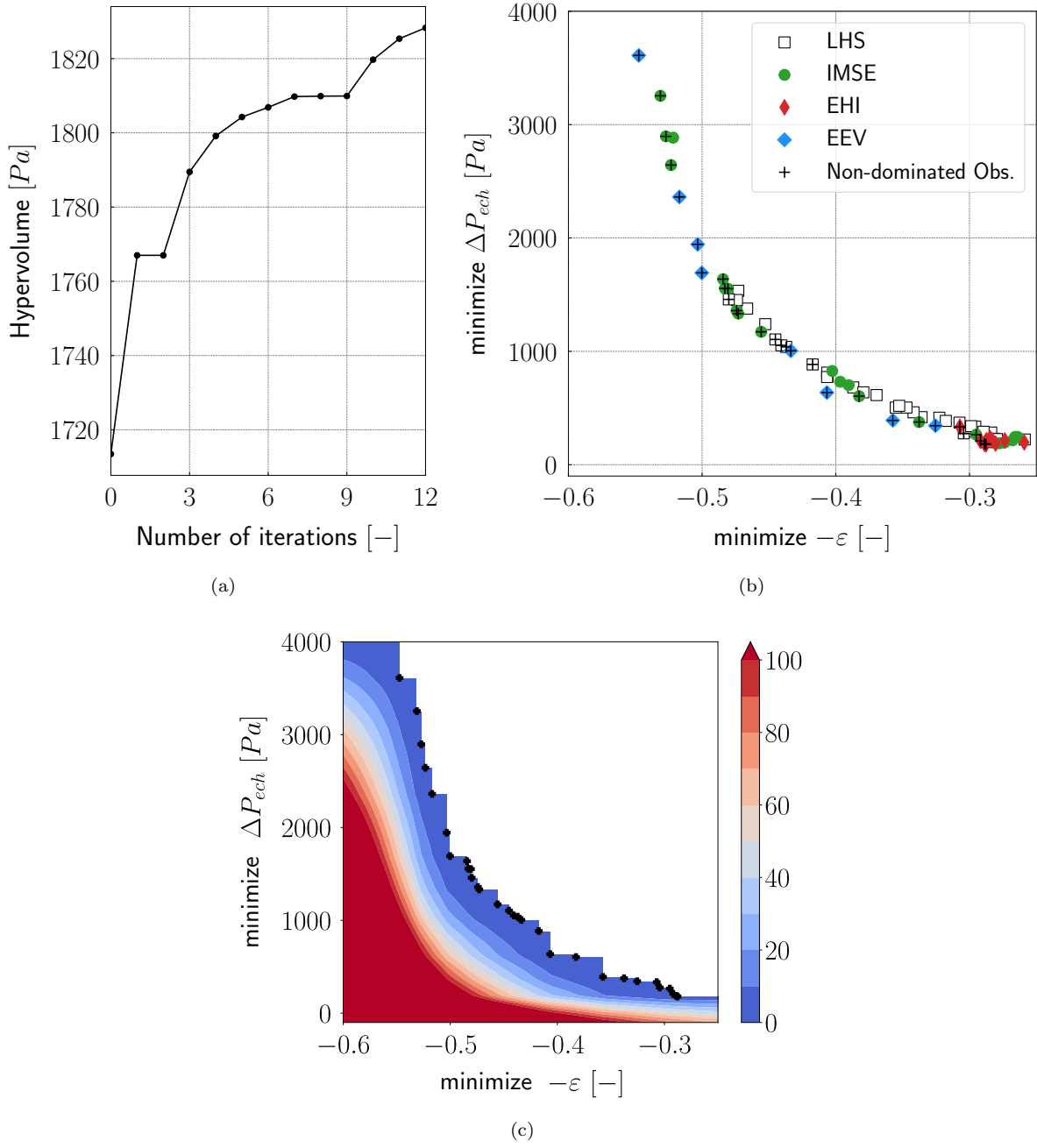


Figure 18: Adaptive sampling results - (a) Hypervolume indicator evolution against the number of iterations (iteration 0 represent the initial LHS) - (b) Observations repartition into the objective space - (c) Contour plot of the hypervolume improvement function Eqn. (30), with non-dominated observations as black dots.

and $\Delta P_{ech} = 3500$ Pa is triggering the sudden increase of the hypervolume at the iteration 10. This criterion is particularly efficient in terms of exploitation, since each added observation is non-dominated and probably belongs

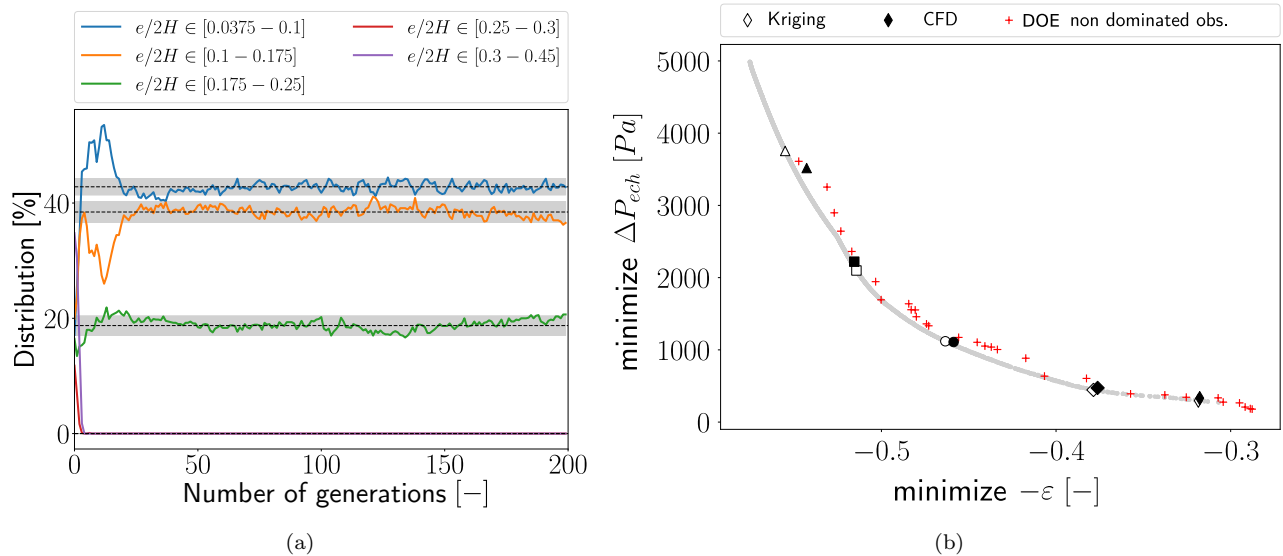


Figure 19: Optimization results - (a) Individuals distribution over generations for the parameter $e/2H$ - (b) Pareto front where the open symbols represent the cluster centres performances predicted by the metamodells, while filled symbols are the performances calculated by CFD simulations. The non-dominated observations are indicated by red crosses. The Pareto front obtained by the NSGA-II is indicated by the grey line.

to the Pareto Front. The left part of the objective space ($-\varepsilon \leq -0.5$) seems to be under-sampled, confirming that the enrichment is not complete.

The three metamodells have been finally built based on the DOE obtained through the adaptive sampling. For all of them, the relative quality indicators computed from the cross-validation are below 3%. Therefore, the metamodells are considered sufficiently accurate to successfully perform the optimization.

5.3 Step 2: Optimization results

The NSGA-II optimization has been carried out using 900 individuals over 200 generations. In order to assess the results, the convergence of this optimization has to be studied. Usually, this is verified by the stability of the Pareto front over the generations in the objective space [78]. However, as the shape optimization is being investigated in the present work, analysing the convergence of the optimal shapes is mandatory [48]. This is done by looking at the distribution of the Pareto front individuals into several classes of the parameters values over the generations. Fig. 19(a) shows this distribution for the rib top width ($e/2H$). As can be seen, the class repartition does not change after the 50th generation. The 95% confident bounds (grey areas) are less than 5% of the mean value (dashed line). Thus the solution given by the NSGA-II is assumed stabilized.

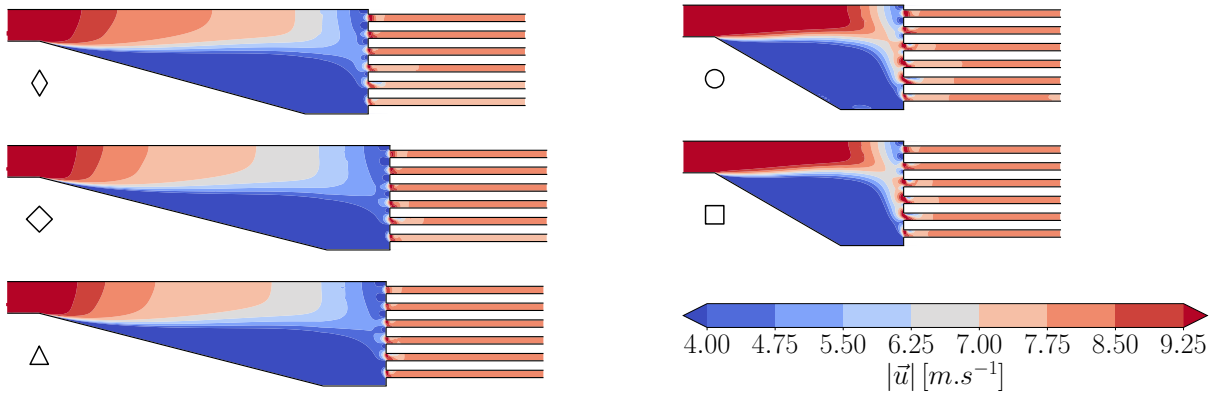
The optimization results are shown in Fig. 19(b). The Pareto front (grey line) is close to the non-dominated observations of the DOE (red crosses). It clearly reveals the antagonistic behaviour of each objective: increasing the effectiveness causes an increase of the pressure drop. Actually, the increase of ε is usually achieved by generating recirculations which in turn increase the pressure losses. The clustering of the individuals highlights five *centres of group* for five different shapes. Their performances predicted by the metamodels are indicated by the open symbols in Fig. 19(b). Extra CFD simulations have been performed *a posteriori* to qualify the metamodels approximation for these centres. The obtained performances are shown as filled symbols in Fig. 19(b). Tab. 5 summarizes the information for each centre: parameters values, CFD performances and differences between the metamodels predictions and the CFD simulations. The difference for the effectiveness is small, with a mean value lower than 1%. The maximum value is reached for the centre Δ , located into the under-sampled zone of the parameter space. The difference is greater for the pressure drop, probably due to the large variation range of this objective.

Table 5: Comparison between metamodels predictions and CFD simulations for the five centres.

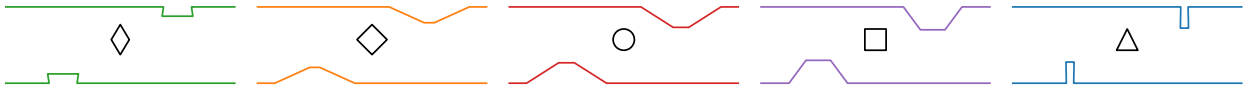
Center	Parameters				CFD performances			Difference metamodels/simulations [%]			
	h_{rib}/H	$e/2H$	\tilde{E}	L_D/H_{in}	$-\varepsilon$ [-]	ΔP_{ech} [Pa]	Υ [%]	$-\varepsilon$	ΔP_{ech}	Mean	Standard deviation
\diamond	0.1219	0.2014	0.006	4.2195	-0.32	331	3.5	0.5	10	$-\varepsilon$	
\diamond	0.2072	0.0666	0.99	4.5664	-0.376	473	1.8	0.63	5.9	0.88	0.75
\circ	0.2678	0.1028	0.99	2.0000	-0.46	1108	2.6	1.0	0.9		
\square	0.2999	0.1612	0.63	2.0000	-0.52	2220	1.8	0.24	5.5	ΔP_{ech}	
Δ	0.2778	0.0534	0	4.5098	-0.54	3516	0.1	2.3	6.7	5.9	3.0

The five optimal shapes obtained by clustering are shown in Fig. 20. Fig. 20(a) represents the diffuser shape together with the mean velocity field. The recirculation area is indicated by the low-speed area (in blue). Fig. 20(b) shows the five ribs shapes, coloured by groups as in Fig. 21.

In order to analyse simultaneously all the information, the Self-Organizing Maps of Fig. 21 are used. In that figure, the four parameters, the two objectives, the standard deviation of the distribution and the five groups obtained by the clustering are represented. The \tilde{E} parameter has been replaced by the angle ψ , more meaningful (see Fig. 6). The two objective maps highlight the previously mentioned antagonistic behaviour, since each is the opposite of the other. The most influential parameter is the rib height (h_{rib}/H): when it is large (centres Δ , \square and \circ) the effectiveness and the pressure drop are important. The visible transition from the blue group (Δ) to the red and purple ones (\square and \circ) is due to a change in the diffuser length (L_D/H_{in}) from its maximum to its minimum value. The other visible transition in the maps is due to the angle (ψ) variation between 90 deg (group Δ) and 120 deg (group \circ). The rib shapes leading to the smaller pressure drop are only slightly different from a flat plate. Indeed, the group denoted by the centre \diamond is characterized by a minimal height and an large rib top width ($e/2H$)



(a)



(b)

Figure 20: Optimal shapes obtained by clustering - (a) diffuser and mean velocity - (b) ribs shape.

as visible in Fig. 20. The group \diamond is formed by ribs of small top width and large angles. Looking at these shapes, it is possible to correlate the global optima to the local optima. Indeed the low pressure shape (centre \diamond) is similar to the low C_f shape highlighted in Fig. 14(b) on the left area (dark blue). Moreover, the high efficiency shape (centre Δ) characterized by important height and small widths is similar to the high Nusselt number shape highlighted in Fig. 14(a).

The distribution standard deviation map highlights the mass flow rate homogeneity among channels of the CPHX. In practice, engineers prefer large diffuser lengths because they are more likely to lead to good distributions. This assumption may be confirmed by analysing the Υ and L_D/H_{in} maps. The centre Δ is characterised by maximal diffuser length (L_D/H_{in}) and minimal value of Υ . Note that some Υ values presented on the map are negative due to the metamodel approximation. However, the CFD results presented in Tab. 5 shows a low value, suggesting that the metamodel provides a good trend if not of exact values. A dedicated adaptive sampling would be necessary here to increase the prediction accuracy or Υ .

A special attention should be given to the centres \square and \diamond which yield the same distribution standard deviation ($\Upsilon = 1.8\%$). However, as shown in Fig. 20(a), the heat exchanger geometry is quite different. The centre \square has a short diffuser, leading to a huge recirculation. This recirculation zone may create a blockage as well as an under-

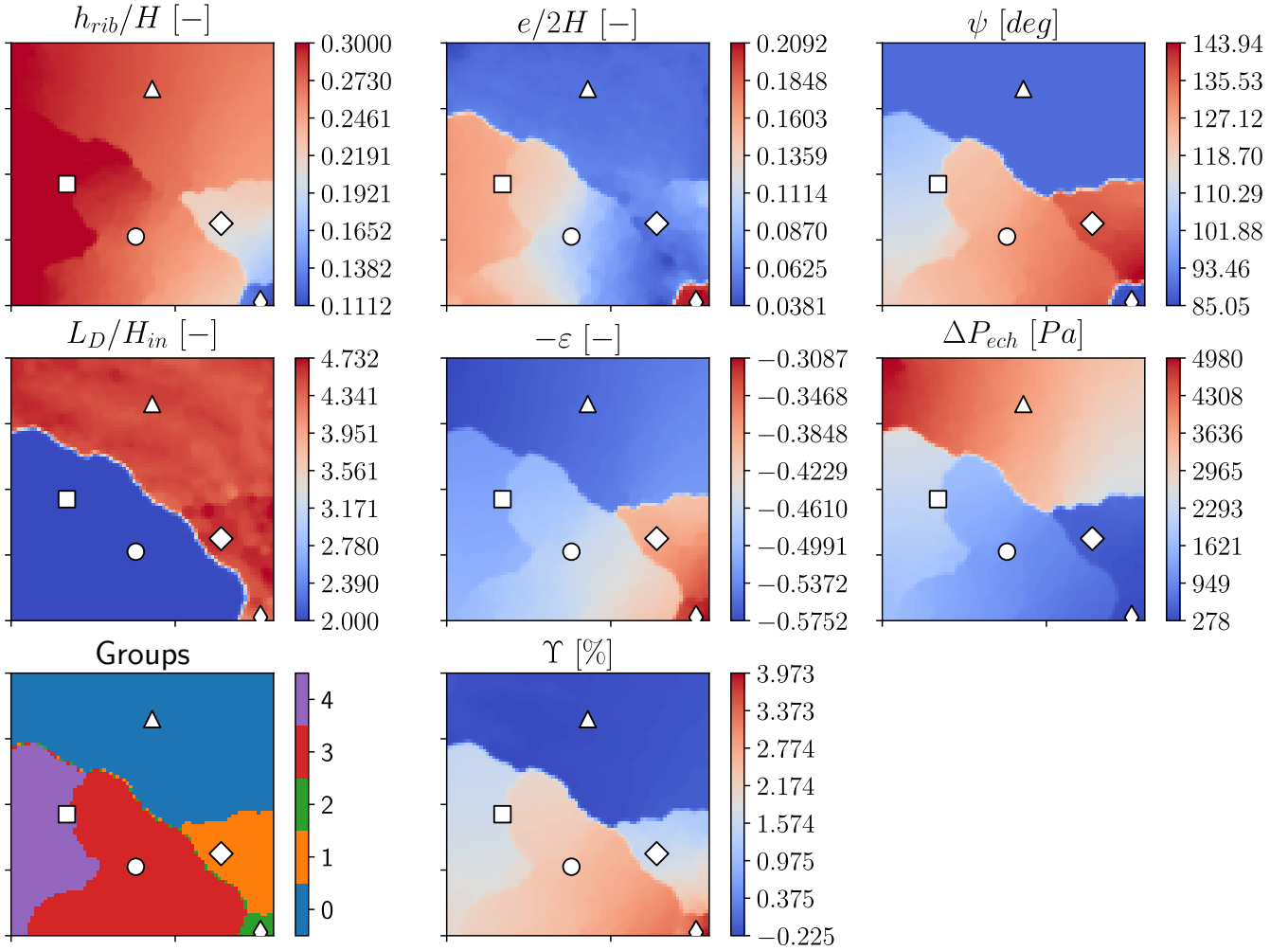


Figure 21: Self-Organizing Maps: the three parameters of the ribs shape (top row); the diffuser length parameter and the two objectives (middle row); the groups generated by the clustering step and the distribution standard deviation (bottom row).

distribution of the lower channels. Nevertheless, as the local rib shape is characterized by a maximal height, the pressure drop in the active part is important. This phenomenon equilibrates the mass flow rate among channels, like a porous media would do. On the contrary, the local shape of the centre \diamond does not lead to a large pressure drop and the homogenous distribution is the consequence of the long diffuser. Obviously, the obtained total pressure drop for the center \square is higher than the \diamond one, as shown by the ΔP_{ech} map on Fig. 21.

This constitutes a valuable finding for the design of heat exchangers revealing that local and global shapes have a coupled influence on the heat exchanger performances.

6. CONCLUSION

The present work has demonstrated that the proposed optimization strategy is relevant for heat exchanger design. The use of CFD simulations allows to overcome the limitations of the experimental correlations. Additionally, metamodels associated with a genetic algorithm enable to apply this strategy to an industrial context with limited numerical and/or time resources. Results have shown the importance of considering conjointly the local and global shapes for the optimization. This has been pointed out by the distribution analyses.

The Kriging metamodeling step is a key element of the present method. It reduces the numerical cost of the optimization and allows to build the correlations used in the multi-scale modelling. Moreover it ensures stability and robustness of the method thanks to nugget effects. This greatly increases the usability of the method in combination with CFD approach. The adaptive sampling strategy is essential to reduce the number of simulations required to build the design of experiment. Furthermore, by combining different infill criteria it is possible to overcome their limitations. This has been the case in the present work for the EHI criterion which is sensitive to the objectives scale.

The clustering limits the number of results to investigate and the Self-Organizing Maps allow to easily correlate the variations of the objectives with the parameters. This is of paramount interest for industrial purpose in order to limit the work remaining after the optimization process and to lay a solid foundation on how each parameter impacts the outcomes.

ACKNOWLEDGEMENT

The authors would like to thank VALEO Thermal Systems BG who provided funding for this research, and EDF R&D for his support on the use of *Code_Saturne*.

REFERENCES

- [1] Abdelaziz, O., Aute, V., Azarm, S. and Radermacher, R. [2010], “Approximation-assisted optimization for novel compact heat exchanger designs”, *HVAC&R Research*, vol. 16, no. 5, pp. 707–728.
- [2] Aubert, S., Mastripolito, F., Rendu, Q., Buisson, M. and Ducros, F. [2017], “Planar Slip Condition For Mesh Morphing Using Radial Basis Functions”, *Procedia Engineering*, vol. 203, pp. 349 – 361, 26th International Meshing Roundtable, IMR26, 18-21 September 2017, Barcelona, Spain.
URL: <http://www.sciencedirect.com/science/article/pii/S1877705817343825>
- [3] Bergman, T.L., Lavine, A.S., Incropera, F.P. and Dewitt, D.P. [2011], *Fundamentals of heat and mass transfer - 7th Edition*, John Wiley & Sons New York.

- [4] Bhutta, M.M.A., Hayat, N., Bashir, M.H., Khan, A.R., Ahmad, K.N. and Khan, S. [2012], “CFD applications in various heat exchangers design: A review”, *Applied Thermal Engineering*, vol. 32, pp. 1–12.
- [5] Billard, F. and Laurence, D. [2012], “A robust $k - \varepsilon - \overline{v^2}/k$ elliptic blending turbulence model applied to near-wall, separated and buoyant flows”, *International Journal of Heat and Fluid Flow*, vol. 33, no. 1, pp. 45–58.
- [6] Binois, M. and Picheny, V. [2016], “GPareto: An R Package for Gaussian-Process Based Multi-Objective Optimization and Analysis”, .
- [7] Bishop, C. [2006], *Pattern Recognition and Machine Learning*, Springer New York.
- [8] Brochu, E., Cora, V.M. and de Freitas, N. [2010], “A tutorial on Bayesian optimization of expensive cost functions, with application to active user modeling and hierarchical reinforcement learning”, Tech. rep., Department of Computer Science, University of British Columbia.
- [9] Buisson, M., Ferrand, P., Soulat, L., Aubert, S., Moreau, S., Rambeau, C. and Henner, M. [2013], “Optimal design of an automotive fan using the TurbOpty meta-model”, *Computers & Fluids*, vol. 80, pp. 207–213.
- [10] Bulliard-Sauret, O., Berindei, J., Ferrouillat, S., Vignal, L., Memponteil, A., Poncet, C., Leveque, J. and Gondrexon, N. [2019], “Heat transfer intensification by low or high frequency ultrasound: Thermal and hydrodynamic phenomenological analysis”, *Experimental Thermal and Fluid Science*, vol. 104, pp. 258 – 271.
URL: <http://www.sciencedirect.com/science/article/pii/S0894177718311427>
- [11] Chevalier, C., Picheny, V. and Ginsbourger, D. [2014], “KrigInv: An efficient and user-friendly implementation of batch-sequential inversion strategies based on kriging”, *Computational statistics & data analysis*, vol. 71, pp. 1021–1034.
- [12] Damblin, G., Couplet, M. and Iooss, B. [2013], “Numerical studies of space-filling designs: optimization of Latin Hypercube Samples and subprojection properties”, *Journal of Simulation*, vol. 7, no. 4, pp. 276–289.
- [13] Deb, K. [1995], *Optimization for engineering design: Algorithms and examples*, PHI Learning Pvt. Ltd., tenth Printing (May 2009).
- [14] Deb, K. [2001], *Multi-objective optimization using evolutionary algorithms*, vol. 16, John Wiley & Sons.
- [15] Deb, K., Pratap, A., Agarwal, S. and Meyarivan, T. [2002], “A fast and elitist multiobjective genetic algorithm: NSGA-II”, *IEEE transactions on evolutionary computation*, vol. 6, no. 2, pp. 182–197.
- [16] Dehoux, F. [2012], *Modélisation statistique des écoulements turbulents en convection forcée, mixte et naturelle*, Ph.D. thesis, Poitiers.

- [17] Dupuy, D., Helbert, C., Franco, J. *et al.* [2015], “DiceDesign and DiceEval: Two R packages for design and analysis of computer experiments”, *Journal of Statistical Software*, vol. 65, no. 11, pp. 1–38.
- [18] El-Behery, S.M. and Hamed, M.H. [2011], “A comparative study of turbulence models performance for separating flow in a planar asymmetric diffuser”, *Computers & Fluids*, vol. 44, no. 1, pp. 248 – 257.
URL: <http://www.sciencedirect.com/science/article/pii/S0045793011000168>
- [19] Emmerich, M.T., Deutz, A.H. and Klinkenberg, J.W. [2011], “Hypervolume-based expected improvement: Monotonicity properties and exact computation”, in *Evolutionary Computation (CEC), 2011 IEEE Congress on*, IEEE, 2147–2154.
- [20] Emmerich, M.T., Giannakoglou, K.C. and Naujoks, B. [2006], “Single-and multiobjective evolutionary optimization assisted by Gaussian random field metamodells”, *IEEE Transactions on Evolutionary Computation*, vol. 10, no. 4, pp. 421–439.
- [21] EDF R&D [2018], “Code_Saturne version 5-1 Theory Guide”, Available online at <https://www.code-saturne.org/cms/sites/default/files/docs/5.1/theory.pdf>.
- [22] Forrester, A.I. and Keane, A.J. [2009], “Recent advances in surrogate-based optimization”, *Progress in Aerospace Sciences*, vol. 45, no. 1-3, pp. 50–79.
- [23] Foundation, P.S. [????], “Python Language Reference, version 2.7.”, <https://www.python.org/>.
- [24] Ghosh, A. and Dehuri, S. [2004], “Evolutionary Algorithms for Multi-Criterion Optimization: A Survey”, *International Journal of Computing & Information Sciences*, vol. 2, no. 1, pp. 38–57.
- [25] Ginsbourger, D., Le Riche, R. and Carraro, L. [2010], “Kriging is well-suited to parallelize optimization”, in *Computational Intelligence in Expensive Optimization Problems*, Springer, 131–162.
- [26] Hajabdollahi, H., Tahani, M. and Fard, M.S. [2011], “CFD modeling and multi-objective optimization of compact heat exchanger using CAN method”, *Applied Thermal Engineering*, vol. 31, no. 14, pp. 2597–2604.
- [27] Han, J.C., Glicksman, L. and Rohsenow, W. [1978], “An investigation of heat transfer and friction for rib-roughened surfaces”, *International Journal of Heat and Mass Transfer*, vol. 21, no. 8, pp. 1143–1156.
- [28] Hilbert, R., Janiga, G., Baron, R. and Thévenin, D. [2006], “Multi-objective shape optimization of a heat exchanger using parallel genetic algorithms”, *International Journal of Heat and Mass Transfer*, vol. 49, no. 15, pp. 2567–2577.
- [29] Huang, D., Allen, T.T., Notz, W.I. and Zeng, N. [2006], “Global Optimization of Stochastic Black-Box Systems via Sequential Kriging Meta-Models”, *Journal of Global Optimization*, vol. 34, no. 3, pp. 441–466.
URL: <https://doi.org/10.1007/s10898-005-2454-3>

- [30] Huang, Y., Liu, Z., Lu, G. and Yu, X. [2014], “Multi-scale thermal analysis approach for the typical heat exchanger in automotive cooling systems”, *International Communications in Heat and Mass Transfer*, vol. 59, pp. 75–87.
- [31] Jiji, L.M. [2002], *Heat Transfer Essentials*, chap. Chap. 9, 2nd ed., Begell House, New York.
- [32] Jones, D.R., Schonlau, M. and Welch, W.J. [1998], “Efficient Global Optimization of Expensive Black-Box Functions”, *Journal of Global Optimization*, vol. 13, no. 4, pp. 455–492.
URL: <https://doi.org/10.1023/A:1008306431147>
- [33] Jouhaud, J.C., Sagaut, P., Montagnac, M. and Laurenceau, J. [2007], “A surrogate-model based multidisciplinary shape optimization method with application to a 2D subsonic airfoil”, *Computers & Fluids*, vol. 36, no. 3, pp. 520–529.
- [34] Keshmiri, A., Osman, K., Benhamadouche, S. and Shokri, N. [2016], “Assessment of advanced RANS models against large eddy simulation and experimental data in the investigation of ribbed passages with passive heat transfer”, *Numerical Heat Transfer, Part B: Fundamentals*, pp. 1–15.
- [35] Kim, H.M., Moon, M.A. and Kim, K.Y. [2011], “Multi-objective optimization of a cooling channel with staggered elliptic dimples”, *Energy*, vol. 36, no. 5, pp. 3419 – 3428.
URL: <https://www.sciencedirect.com/science/article/pii/S0360544211002118>
- [36] Kim, K.Y. and Choi, J.Y. [2005], “Shape optimization of a dimpled channel to enhance turbulent heat transfer”, *Numerical Heat Transfer, Part A: Applications*, vol. 48, no. 9, pp. 901–915.
- [37] Kohonen, T. [1982], “Self-organized formation of topologically correct feature maps”, *Biological Cybernetics*, vol. 43, no. 1, pp. 59–69.
URL: <https://doi.org/10.1007/BF00337288>
- [38] Koo, G.W., Lee, S.M. and Kim, K.Y. [2014], “Shape optimization of inlet part of a printed circuit heat exchanger using surrogate modeling”, *Applied Thermal Engineering*, vol. 72, no. 1, pp. 90 – 96, {ASCHT2013}.
URL: <https://www.sciencedirect.com/science/article/pii/S1359431113008867>
- [39] Liu, C., Bu, W. and Xu, D. [2017], “Multi-objective shape optimization of a plate-fin heat exchanger using CFD and multi-objective genetic algorithm”, *International Journal of Heat and Mass Transfer*, vol. 111, pp. 65 – 82.
- [40] Liu, C., Deng, Y., Wang, X., Liu, X., Wang, Y. and Su, C. [2016], “Multi-objective optimization of heat exchanger in an automotive exhaust thermoelectric generator”, *Applied Thermal Engineering*, vol. 108, pp. 916 – 926.
URL: <https://www.sciencedirect.com/science/article/pii/S1359431116313163>

- [41] Liu, J., Han, Z. and Song, W. [2012], “Comparison of infill sampling criteria in kriging-based aerodynamic optimization”, in *28th Congress of the International Council of the Aeronautical Sciences*, 23–28.
- [42] Liu, J., Song, W.P., Han, Z.H. and Zhang, Y. [2017], “Efficient aerodynamic shape optimization of transonic wings using a parallel infilling strategy and surrogate models”, *Structural and Multidisciplinary Optimization*, vol. 55, no. 3, pp. 925–943.
- [43] Maghsoudi, P., Sadeghi, S., Khanjarpanah, H. and Gorgani, H.H. [2018], “A comprehensive thermo-economic analysis, optimization and ranking of different microturbine plate-fin recuperators designs employing similar and dissimilar fins on hot and cold sides with NSGA-II algorithm and DEA model”, *Applied Thermal Engineering*, vol. 130, no. Supplement C, pp. 1090 – 1104.
URL: <http://www.sciencedirect.com/science/article/pii/S1359431117356521>
- [44] Manceau, R., Parneix, S. and Laurence, D. [2000], “Turbulent heat transfer predictions using the v2-f model on unstructured meshes”, *International Journal of Heat and Fluid Flow*, vol. 21, no. 3, pp. 320–328.
- [45] Manglik, R.M. [2003], *Heat Transfer Enhancement*, chap. 14, John Wiley & Sons, 1129 – 1130.
- [46] Marler, R.T. and Arora, J.S. [2004], “Survey of multi-objective optimization methods for engineering”, *Struct. Multidiscip. Optim.*, vol. 26, no. 6, pp. 369–395.
URL: <http://link.springer.com/10.1007/s00158-003-0368-6>
- [47] Mastrippolito, F., Aubert, S., Ducros, F. and Buisson, M. [2019], “RBF-based mesh morphing improvement using Schur complement applied to rib shape optimization (Soumis)”, *International Journal of Numerical Methods for Heat and Fluid Flow*.
- [48] Mastrippolito, F., Aubert, S., Ducros, F., Ferrand, M. and Fourmigue, J.F. [2018], “Multi-objective shape optimization of a plate heat exchanger : a multi-scale Approach”, in *International Conference on Energy Engineering and Smart Grids, 25-26 Juin 2018, Cambridge, United Kingdom*.
- [49] Mebane Jr, W.R., Sekhon, J.S. *et al.* [2011], “Genetic optimization using derivatives: the rgenoud package for R”, *Journal of Statistical Software*, vol. 42, no. 11, pp. 1–26.
- [50] Menter, F.R. [1994], “Two-equation eddy-viscosity turbulence models for engineering applications”, *AIAA journal*, vol. 32, no. 8, pp. 1598–1605.
- [51] Messac, A., Puemi-Sukam, C. and Melachrinoudis, E. [2000], “Aggregate Objective Functions and Pareto Frontiers: Required Relationships and Practical Implications”, *Optimization and Engineering*, vol. 1, no. 2, pp. 171–188.

- [52] Mishra, M., Das, P. and Sarangi, S. [2009], “Second law based optimisation of crossflow plate-fin heat exchanger design using genetic algorithm”, *Applied Thermal Engineering*, vol. 29, no. 14, pp. 2983 – 2989.
URL: <http://www.sciencedirect.com/science/article/pii/S1359431109000945>
- [53] Missirlis, D., Donnerhack, S., Seite, O., Albanakis, C., Sideridis, A., Yakinthos, K. and Goulas, A. [2010], “Numerical development of a heat transfer and pressure drop porosity model for a heat exchanger for aero engine applications”, *Applied Thermal Engineering*, vol. 30, no. 11-12, pp. 1341–1350.
- [54] Mohammadi, H. [2016], *Kriging-based black-box global optimization: analysis and new algorithms*, Ph.D. thesis, Ecole Nationale Supérieure des Mines de Saint-Etienne.
- [55] Moosavi, V., Packmann, S. and Valls, I. [2018], “SOMPY : A Python Library for Self Organizing Map.”, Available from <https://github.com/sevamoo/SOMPY>.
- [56] Musto, M., Bianco, N., Rotondo, G., Toscano, F. and Pezzella, G. [2016], “A simplified methodology to simulate a heat exchanger in an aircraft’s oil cooler by means of a porous media model”, *Applied Thermal Engineering*, vol. 94, pp. 836–845.
- [57] Park, J.S. and Baek, J. [2001], “Efficient computation of maximum likelihood estimators in a spatial linear model with power exponential covariogram”, *Computers & Geosciences*, vol. 27, no. 1, pp. 1–7.
- [58] Park, K., Oh, P.K. and Lim, H.J. [2006], “The application of the {CFD} and Kriging method to an optimization of heat sink”, *International Journal of Heat and Mass Transfer*, vol. 49, no. 1920, pp. 3439 – 3447.
URL: <https://www.sciencedirect.com/science/article/pii/S0017931006002055>
- [59] Patankar, S., Liu, C. and Sparrow, E. [1977], “Fully developed flow and heat transfer in ducts having streamwise-periodic variations of cross-sectional area”, *ASME J. Heat Transfer*, vol. 99, no. 2, pp. 180–186.
- [60] Pedregosa, F., Varoquaux, G., Gramfort, A., Michel, V., Thirion, B., Grisel, O., Blondel, M., Prettenhofer, P., Weiss, R., Dubourg, V., Vanderplas, J., Passos, A., Cournapeau, D., Brucher, M., Perrot, M. and Duchesnay, E. [2011], “Scikit-learn: Machine Learning in Python”, *Journal of Machine Learning Research*, vol. 12, pp. 2825–2830.
- [61] Picheny, V. [2015], “Multiobjective optimization using Gaussian process emulators via stepwise uncertainty reduction”, *Statistics and Computing*, vol. 25, no. 6, pp. 1265–1280.
- [62] Picheny, V., Ginsbourger, D., Roustant, O., Haftka, R.T. and Kim, N.H. [2010], “Adaptive designs of experiments for accurate approximation of a target region”, *Journal of Mechanical Design*, vol. 132, no. 7, p. 071008.

- [63] Ponweiser, W., Wagner, T. and Vincze, M. [2008], “Clustered multiple generalized expected improvement: A novel infill sampling criterion for surrogate models”, in *Evolutionary Computation, 2008. CEC 2008.(IEEE World Congress on Computational Intelligence). IEEE Congress on, IEEE*, 3515–3522.
- [64] R Core Team [2012], *R: A Language and Environment for Statistical Computing*, R Foundation for Statistical Computing, Vienna, Austria, ISBN 3-900051-07-0.
URL: <http://www.R-project.org/>
- [65] Rau, G., Cakan, M., Moeller, D. and Arts, T. [1998], “The Effect of Periodic Ribs on the Local Aerodynamic and Heat Transfer Performance of a Straight Cooling Channel”, *Journal of Turbomachinery*, vol. 120, no. 2, pp. 368–375.
- [66] Roustant, O., Ginsbourger, D. and Deville, Y. [2012], “DiceKriging, DiceOptim: Two R Packages for the Analysis of Computer Experiments by Kriging-Based Metamodeling and Optimization”, *Journal of statistical software*, vol. 51, no. 1, pp. 1–55.
- [67] Sacks, J., Schiller, S.B. and Welch, W.J. [1989], “Designs for computer experiments”, *Technometrics*, vol. 31, no. 1, pp. 41–47.
- [68] Sacks, J., Welch, W.J., Mitchell, T.J. and Wynn, H.P. [1989], “Design and analysis of computer experiments”, *Statistical science*, pp. 409–423.
- [69] Saleh, K., Abdelaziz, O., Aute, V., Radermacher, R. and Azarm, S. [2013], “Approximation assisted optimization of headers for new generation of air-cooled heat exchangers”, *Applied Thermal Engineering*, vol. 61, no. 2, pp. 817 – 824.
URL: <https://www.sciencedirect.com/science/article/pii/S1359431112004279>
- [70] Saleh, K., Aute, V., Radermacher, R. and Azarm, S. [2013], “Chevron plate heat exchanger optimization using efficient approximation-assisted multi-objective optimization techniques”, *HVAC&R Research*, vol. 19, no. 7, pp. 788–799.
- [71] Sanaye, S. and Hajabdollahi, H. [2010], “Multi-objective optimization of shell and tube heat exchangers”, *Applied Thermal Engineering*, vol. 30, no. 14, pp. 1937 – 1945.
URL: <http://www.sciencedirect.com/science/article/pii/S135943111000181X>
- [72] Sanaye, S. and Hajabdollahi, H. [2010], “Thermal-economic multi-objective optimization of plate fin heat exchanger using genetic algorithm”, *Applied Energy*, vol. 87, no. 6, pp. 1893 – 1902.
URL: <http://www.sciencedirect.com/science/article/pii/S0306261909005030>
- [73] Sasena, M.J., Papalambros, P. and Goovaerts, P. [2002], “Exploration of metamodeling sampling criteria for constrained global optimization”, *Engineering optimization*, vol. 34, no. 3, pp. 263–278.

- [74] Shah, R.K. and Sekulic, D.P. [2003], *Fundamentals of heat exchanger design*, John Wiley & Sons.
- [75] Shi, H., Ma, T., xiao Chu, W. and wang Wang, Q. [2017], “Optimization of inlet part of a microchannel ceramic heat exchanger using surrogate model coupled with genetic algorithm”, *Energy Conversion and Management*, vol. 149, pp. 988 – 996.
URL: <https://www.sciencedirect.com/science/article/pii/S019689041730345X>
- [76] Shimoyama, K., Sato, K., Jeong, S. and Obayashi, S. [2012], “Comparison of the criteria for updating kriging response surface models in multi-objective optimization”, in *Evolutionary Computation (CEC), 2012 IEEE Congress on*, IEEE, 1–8.
- [77] Sleijpen, G.L. and Fokkema, D.R. [1993], “BiCGstab (l) for linear equations involving unsymmetric matrices with complex spectrum”, *Electronic Transactions on Numerical Analysis*, vol. 1, no. 11, p. 2000.
- [78] Soulat, L., Ferrand, P., Moreau, S., Aubert, S. and Buisson, M. [2013], “Efficient optimisation procedure for design problems in fluid mechanics”, *Computers & Fluids*, vol. 82, pp. 73 – 86.
URL: <http://www.sciencedirect.com/science/article/pii/S0045793013001497>
- [79] Sundén, B. [2007], “Computational fluid dynamics in research and design of heat exchangers”, *Heat Transfer Engineering*, vol. 28, no. 11, pp. 898–910.
- [80] Svenson, J. [2011], *Computer experiments: Multiobjective optimization and sensitivity analysis*, Ph.D. thesis, The Ohio State University.
- [81] Tanda, G. [2004], “Heat transfer in rectangular channels with transverse and V-shaped broken ribs”, *International Journal of Heat and Mass Transfer*, vol. 47, no. 2, pp. 229–243.
- [82] Thulukkanam, K. [2013], *Heat exchanger design handbook*, CRC Press.
- [83] Tušar, T. and Filipič, B. [2015], “Visualization of Pareto front approximations in evolutionary multiobjective optimization: A critical review and the prosection method”, *IEEE Transactions on Evolutionary Computation*, vol. 19, no. 2, pp. 225–245.
- [84] Viana, F.A. [2013], “Things you wanted to know about the Latin hypercube design and were afraid to ask”, in *10th World Congress on Structural and Multidisciplinary Optimization*, sn, 1–9.
- [85] Villemonteix, J., Vazquez, E. and Walter, E. [2009], “An informational approach to the global optimization of expensive-to-evaluate functions”, *Journal of Global Optimization*, vol. 44, no. 4, p. 509.
- [86] Wen, J., Yang, H., Tong, X., Li, K., Wang, S. and Li, Y. [2016], “Configuration parameters design and optimization for plate-fin heat exchangers with serrated fin by multi-objective genetic algorithm”, *Energy Conversion and Management*, vol. 117, pp. 482–489.

- [87] Yin, H. and Ooka, R. [2015], “Shape optimization of water-to-water plate-fin heat exchanger using computational fluid dynamics and genetic algorithm”, *Applied Thermal Engineering*, vol. 80, pp. 310–318.